Pressure propagation through the bed in the swash zone of a sandy beach

A data and modelling study with possible implications for sediment transport

UNIVERSITY OF TWENTE.

Master thesis
T. Pauli (s1553461)
Faculty of Engineering Technology
MSc River and Coastal Engineering
03-07-2020

The cover page image is retrieved from Flickr Versageek, undertow

Preface

I hereby proudly present my thesis that I worked on the previous months. This is the final product of the River and Coastal Engineering master at the University of Twente.

I would like to thank a couple of people who where of great help during the research. First, I would like to give my gratitude to my daily supervisor Joost who weekly supported me and extensively thought along with the challenges during the study. Secondly, I would like to thank Jebbe for his input on the swash zone dynamics. Furthermore, I would like to thank Kathelijne for the supervision and critical view on the research. Finally, I would give my gratitude to Niels Jacobsen who shared his expertise on the topic and new insights in the research approach.

Please enjoy reading!

Abstract

To ensure flood safety, it is important to acquire knowledge on coastal development. The morphology of the coast changes by sediment transport under wave forcing conditions. One of the most important coastal areas where sediment is transported, is the swash zone of a beach. The swash zone is the nearshore part of the beach, intermittently covered by water and exposed to the air, due to wave uprush and backwash. Pressure propagates through the bed as a response to the waves with a pressure amplitude attenuation and phase lag, by increasing depth. This leads to vertical pressure gradients in the bed, which affect the effective sediment weight. Simultaneously, ventilated boundary layers arise, which stabilize or destabilize the flow velocity at the bed during infiltration or exfiltration, associated with the pressure gradients. A destabilization of the flow velocity will decrease the bed shear stress. In this thesis, the influence of the pressure gradient for both processes and the implication on sediment transport is studied in more detail. In order to achieve this, the pressure propagation will be modelled, to determine the pressure gradients at the bed surface.

A new data set is used, obtained from wave flume experiments, to observe the pressure behaviour and calibrate the model. The data consists of thirty minute runs of bichromatic erosive waves. These runs contain two wave groups of six waves with a target significant wave height of 0.65 m. The pressure is observed at multiple depths in the swash zone of a fine to medium sandy beach, ranging from 0.30-0.65 m depth, under wave forcing conditions.

An exponential pressure amplitude attenuation and a linear phase lag by increasing depth are observed. The pressure propagation velocity through the bed is frequency dependent and is approximately 0.4 m/s for the range of 0.26-0.31 Hz. Upwards directed pressure gradients occur during backwash, associated with exfiltration and downwards directed pressure gradients occur during uprush.

The pressure propagation is modelled, based on the theory of Yamamoto et al. (1978), which is applicable for sea beds, although not found to be applicable for small water depths and dry periods yet. The model is calibrated with the data for one parameter value ($a = 30 - 37.5$), which incorporates the pressure amplitude attenuation and phase lag, based on the soil characteristics. The modelled pressure shows a very high correlation with the observed pressure of $R^2 = 0.96 - 0.99$, Nash Sutcliffe values of $0.90 - 0.99$ and Root Mean Square Errors normalized by the standard deviation of 0.10-0.31.

Subsequently, the model was used to compute the pressure gradients near the bed surface. Two modified Shields formulations are used to determine the implication of the pressure gradients on sediment transport. Francalanci et al. (2008) only incorporate the change in the effective sediment weight and Nielsen et al. (2001) incorporate both the effective sediment weight effect and the ventilated boundary layer effect. These findings show normalized Shields number ratio's up to 1.6 ((Francalanci et al., 2008)) and 1.13 ((Nielsen et al., 2001)) during backwash. Both methods indicate a significant increase in the Shields number, as a consequence of the pressure gradients.

This thesis contributes to the growing applicability of the pressure modelling theory of Yamamoto et al. (1978). The results showed that the theory is also applicable for the swash zone, which is characterized by small water depths and dry periods. Moreover, this study contributes to the implication of the pressure gradients on sediment transport. The findings showed that the effective sediment weight effect is the leading process compared to the ventilated boundary layer effect and significantly influence the dimensionless bed shear stress (Shields number).

Contents

Chapter 1

Introduction

Important processes influencing coastal flood safety need to be fully understood. In coastal environments high water levels and wave forcing are threats for flooding. Knowledge on the environment in front of the dunes can contribute to the design of the flood protection structure. Failure mechanisms, such as overtopping, occur when runup exceeds the crest of the dune. This is one of the many possible failure mechanisms leading to flooding of the hinterland. Simulating the wave conditions and coastal development provides meaningful information needed for the design. This will lead to human interventions to ensure flood safety like nourishments to lower the runup or heighten/widen the dune.

The specific area of interest, in front of the dune, in this study, is the swash zone of a sandy beach. The swash zone is the nearshore dynamic part of the beach, covered and exposed by uprush and backwash of water (Bakhtyar et al., 2009). The morphodynamic system in the swash zone consists of hydrodynamics, morphology and sediment transport (Masselink and Puleo, 2006). Under different hydrodynamic conditions, the morphology of the beach changes by onshore and offshore sediment transport. Many parameters influence this process, among which infiltration/exfiltration, bed slope, turbulence, shear stress and grain size. Sediment transport models incorporate many processes mentioned above to simulate the coastal development. However, for certain processes, the impact on sediment transport is not fully understood. It is believed that the vertical pressure gradient in the soil affects the effective weight of the sediment and/or change the bed shear stress influencing the rate of accretion and erosion (Anderson et al., 2017) (Nielsen et al., 2001) (Francalanci et al., 2008) (Sumer et al., 2011).

The vertical pressure gradient is the pressure difference between different depths in the soil. Studying the pressure propagation with the pressure gradients in the bed of the swash zone helps to reveal the pressure behaviour under interacting wave conditions. The findings could make an important contribution to the more in depth understanding of pressure gradients and the implication on sediment transport in the swash zone.

Previous modelling studies of the pressure propagation through the bed are limited to sea beds with large water depths of a couple of meters and are not proven to be applicable for areas with no inundation (Yamamoto et al., 1978) (Raubenheimer et al., 1998) (Guest and Hay, 2017). Overall, the modelling studies showed promising results for simulating the pressure propagation through the bed. Still, the pressure propagation in the swash zone, characterised by mean water depths of approximately 10-15 cm and dry periods, is not studied extensively.

In this research, a new data set is used which differs from previous studies. The experiment consists of bichromatic waves forcing on an artificial beach for a time period of thirty minutes. Previous studies only consider one or a small number of waves forcing on the beach and therefore the interference between wave groups are not included. It is still not known how the pressure gradients could be modelled and how the pressure gradients behave in the swash zone for interfering wave groups. The purpose of this research is to study the vertical pressure gradients behaviour and modelling approach, more extensively, with the implication on sediment transport in the swash zone.

1.1 Research questions and objective

The aim of this research is to get a better understanding of the vertical pressure gradients and simulate the pressure propagation in the soil of the swash zone with the implication on sediment transport. The main research question is formulated:

How does the vertical pressure distribution in the soil behave under wave forcing conditions in the swash zone of a sandy beach?

The main research question is subdivided into sub-questions:

1. How does the vertical pressure gradient in the bed of the swash zone respond to wave forcing?
2. How can the pressure propagation and gradient in the bed be modelled as a response to the wave forcing?
3. What is the effect of the pressure gradient on the dimensionless bed shear stress (Shields number)?

First, the raw data of the wave flume experiment is processed and analysed. The pressure gradients are determined from the pressure measurements and the outcomes are compared to similar studies (RQ1). Afterwards, a model, calibrated with the observed data, is presented in order to estimate the pressure propagation through the bed depending on the wave surface elevation and soil characteristics to determine the pressure gradients at the bed surface (RQ2). Finally, the modelled pressure gradients in combination with the flow velocity at the bed are used to determine the dimensionless bed shear stress. Multiple modified Shields parametrizations are used, which consists of different processes such as the effective sediment weight and the ventilated boundary layer to evaluate the implication for sediment transport (RQ3).

1.2 Outline report

In the next Chapter, background information is provided to explain the important processes in the swash zone and previously conducted research on this topic. In Chapter 3 the methodology is described, explaining the research approach. In Chapter 4, the results are presented and in Chapter 5, the results are discussed. Finally, conclusions and recommendations are presented in Chapter 6 and 7.

Chapter 2

Theoretical background

In this chapter, a theoretical framework is presented to explain the topics and terminology related to this research. The study area is the swash zone of a sandy beach. The hydrodynamic forcing, the beach groundwater system and sediment transport in the swash zone are described. Pressure propagates through the soil as a response to the hydrodynamic forcing. A theory for the pressure propagation is presented. Finally, the influence of the pressure gradient on the dimensionless bed shear stress is described.

2.1 Hydrodynamics

The swash zone is the nearshore part of the beach intermittently covered by water and exposed to the air due to wave uprush and backwash (Bakhtyar et al., 2009). This dynamic region, where wave energy is dissipated or reflected, closely interacts with the surf zone (Chardón-Maldonado et al., 2016) (Figure 2.1). The surf zone and swash zone morphodynamic system consists of hydrodynamics, morphology and sediment transport which are closely linked together (Masselink and Puleo, 2006).

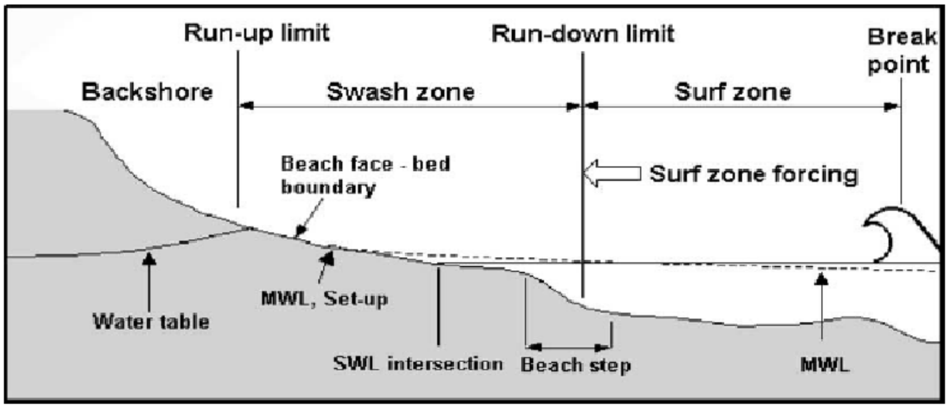

Figure 2.1: Schematization of the swash zone. Based on: Elfrink and Baldock (2002).

The hydrodynamics concern the random onshore and alongshore directed waves from the ocean or sea on the beach. The direction and magnitude of the waves mainly depend on the wind and tide. The hydrodynamics in the swash zone are characterised by interacting waves with small water depths in the order of magnitude of centimeters. The process of incoming waves can be described in detail in a couple of steps (Masselink and Puleo, 2006): (1) a wave is approaching the point of collapse. Turbulence occurs, enhanced by the onshore directed water velocities in the upper part of the water column and offshore directed flow near the bed, (2) the wave collapses resulting in a pressure push leading to a small acceleration of the uprush. Some water might infiltrate the foreshore surface, (3) the flow reached its maximum shorewards position due to the bed slope and friction. The water starts to flow in offshore direction, as backwash, and (4) backwash interacts/collides with the next wave, decelerating the backwash. During backwash, the water will exfiltrate or infiltrate based on the soil characteristics. Backwash durations are typically larger and have shallower water depths than uprush durations. Infiltration increases the swash flow asymmetry by reducing the duration and strength (Masselink and Li, 2001). The difference between the flow velocities between the uprush and backwash is called the asymmetry in the swash zone. The asymmetry determines the direction and magnitude of sediment transport.

Besides the wave forcing on top of the bed surface, the beach groundwater system also plays a role in sediment transport. The beach groundwater system is an unconfined aquifer which responds to tides, waves, evaporation, rainfall and water exchange with deeper aquifers. This results in watertable changes (Figure 2.2). Water, sediment, gas and organic matter between the groundwater, saturated/unsaturated sediment layer and the surface of the beach exchanges. Important parameters such as beach elevation, pore water pressures, hydraulic conductivity (K), drainable porosity and moisture content determine the rate of exchange between these layers.

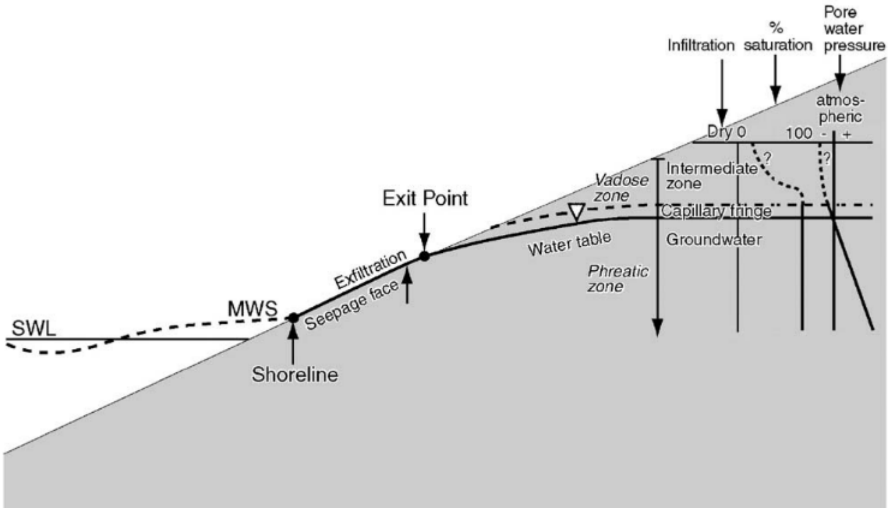

Figure 2.2: Schematization of the beach ground water system. Taken from Horn (2006).

Horizontal groundwater flows (v_h) and vertical groundwater flows (seepage) (v_s) are commonly described by Darcy's law (2.1) (2.2), applicable for laminar flows on sandy beaches. This is a linear relation between the flow velocity and the pressure gradient depending on the hydraulic conductivity:

$$v_h = -K \frac{\partial h}{\partial x} \tag{2.1}$$

and

$$v_s = -\frac{K}{\rho g} \frac{\partial h}{\partial z}, \tag{2.2}$$

where $K(m/s)$ is the permeability and $h(m)$ is the hydraulic head (Horn, 2006). The permeability is highly uncertain and ranges from $K(O(^{-2}) - O(^{-5}))$ for sand. Rosas et al. (2014) studied a variety of methods for the hydraulic conductivity for different environments. For beach environments both the modified method of Hazen (2.3) (Hazen, 1892) and Kozeny-Carman (2.4) (Kozeny, 1927) (Kozeny, 1953) (Carman, 1937) (Carman, 1956) fit well ($R^2 = 0.75$), which are defined as

$$K = A \left(D_{10}\right)^2 \tag{2.3}$$

and

$$K = \beta \frac{\rho g}{\mu} \frac{\epsilon^3}{(1-\epsilon)^2} D_{10}^2, \tag{2.4}$$

where A is a coefficient ranging from 1-1.5 ($m^{-1}s^{-1}$), D_{10} is the 10th percentile grain size and ϵ is the porosity. β is a coefficient of $\frac{1}{180}$.

The porewater pressure in the soil on a beach depends on multiple factors and varies in time due to tidal forcing and wave forcing. Groundwater levels in the swash zone highly determine the porewater pressure, by the total head. Infiltration causes an increase in the watertable while exfiltration decreases the groundwater level. This is an interactive process in the swash cycle changing the groundwater level in order of seconds. The slope of the watertable changes with tide and the surface of the watertable is generally not flat (Horn, 2006). The wave forcing effects could be assigned to time-averaged and single wave impacts. Time-averaged wave forcing induces a watertable overheight, by set-up and run-up, increasing the mean water surface (Horn, 2006). Single wave forcing causes high-frequency watertable fluctuations by the transmission of pressure forces through saturated sediment, swash infiltration and the Wieringermeer effect, explained below. The hydraulic conductivity highly determines the infiltration/exfiltration rate and varies the most in the swash zone of a beach due to the saturation and desaturation of sand. The Wieringermeer effect concerns the appearance and disappearance of meniscuses between sand grains in the capillary fringe of the watertable. When a meniscus appears under negative pressure (tension), water drains into the pores, causing a pressure difference across the air-water interface balancing the negative pressure head. Infiltration from an incoming wave adds a small amount of water releasing the tension and enhancing a watertable rise towards the ground surface (Horn, 2006).

2.2 Sediment transport dynamics

There are two modes of sediment transport: suspended sediment transport and bed load sediment transport. The suspended sediment in the water that stays into suspension due to turbulent eddies outweigh the settling velocity of the particles. Sediment that is transported along the bed forced by waves and currents, is called bed load sediment transport. The amount of sediment transport depends on both the wave forcing and the soil characteristics. The Shields parameter is a widely used method to determine the initiation of motion and transported volume of sediment caused by a flow (Shields, 1936):

$$\theta = \frac{\tau}{(\rho_s - \rho)\, D}, \tag{2.5}$$

where τ is the dimensional shear stress, $\rho_s (kg/m^3)$ is the sediment density, $\rho (kg/m^3)$ is the water density and $D(m)$ is the characteristic particle diameter. The bed shear stress is expressed by (Reniers et al., 2013)

$$\tau_b = \rho c_f |u| u, \tag{2.6}$$

with

$$c_f = \frac{g}{C^2}. \tag{2.7}$$

Under different hydrodynamic conditions the morphology of the beach changes due to onshore and offshore sediment transport. Sediment is transported to the upper or lower part of the beach by uprush and backwash depending on the erosive or accretion character of the waves (Masselink and Puleo, 2006). Approaching waves consist of energy in terms of the flow velocity and wave height, which will be transferred to the beach, leading to sediment transport. Infiltration in the swash zone causes asymmetry in the uprush/backwash flow leading to a change in energy available for sediment transport. Infiltration increases shear stress and skin friction at the bed and exfiltration decreases bed shear stress and friction (Horn, 2006). The shear stress that sets sediment particles in motion highly determining the bed load transport. Shear stresses during uprush are larger, but of a shorter duration compared to backwash (Masselink and Puleo, 2006). Turbulence generated by the wave collapse can reach the bed in the shallow swash zone resulting in sediment taken into suspension (Butt et al., 2004). Therefore, turbulence is a significant parameter in sediment transport (Sumer et al., 2011). Alongshore sediment transport is caused by shoaling and refraction of the approaching waves, changing the wave height and angle. A widely used formula to describe the alongshore sediment transport is the CERC equation, stating a proportional relation between the alongshore wave power and the alongshore transport rate (Waterways Experiment Station, 1984). In this study, alongshore sediment transport is not considered, because the wave flume is small and unable to simulate alongshore processes.

In case the force, caused by the upwards water flow through the porous bed, is larger than the buoyant weight of the grains, the bed could be fluidised. If this occurs, the Shields number no longer is a good representation of sediment transport. This critical threshold for liquefaction needs to be resolved to verify the applicability of the Shields number. Soulsby (1998) presents a method to determine the minimum vertical pressure gradient needed to liquefy the bed, balancing the weight of the grains, with a minimum fluidisation velocity v_{min}, given by

$$\left(\frac{\mathrm{d}p}{\mathrm{d}z}\right)_{\mathrm{v_{min}}} = \mathrm{g}\left(\rho_{\mathrm{s}} - \rho\right)\left(1 - \varepsilon\right), \tag{2.8}$$

where $\rho_{\mathrm{s}}(kg/m^3)$ is the density of the grains, $\rho(kg/m^3)$ is the density of water and $\varepsilon(-)$ is the porosity.

2.3 Pressure propagation and gradients in the soil

Pressure propagates from the bed surface through the bed enhanced by the waves. The pressure amplitude decreases by increasing depth and there is a delay caused by the propagation velocity. The difference between the pressure in between two depths is the pressure gradient. The delay in depth is expressed by the phase lag, which is the delay normalized with the frequency. A large phase lag and a large pressure amplitude attenuation are associated with a large pressure gradient.

Studies regarding the pressure gradient in the soil are listed below. Baldock and Holmes (1996) conducted horizontal and vertical pressure gradient measurements at multiple locations in the surf zone of a laboratory scale beach. The horizontal and vertical pressure gradients are of similar magnitude near the bed. Turner and Nielsen (1997) compared the pressure signals, measured in the field, on three different depths in the swash zone. The results show a high correlation degree ($r^2 > 0.99$) between z=4 cm and z=19 cm with a lag of 0.25 s. Young et al. (2010) simulated tsunami erosion in a wave flume under breaking solitary wave conditions, monitoring the vertical pressure gradient on different depths. During the backwash, intense sediment transport was observed leading to a net erosion of the beach. Anderson et al. (2017) studied the horizontal and vertical pressure gradient on a surfzone sandbar. The study of van der Zanden et al. (2019) suggests that there is no significant relation between the horizontal pressure gradient forces and the growth of the sheet flow layer. Therefore, the horizontal pressure gradient at the surface of the bed is assumed to have no significant importance for sediment transport.

2.4 Pressure propagation theory

Yamamoto et al. (1978) present analytical solutions for the pressure propagation through a porous bed based on the consolidation theory of Biot (1941). For partly saturated soils, the exponential pressure amplitude attenuation and linear phase lag are suggested to be highly dependent on the permeability and the stiffness of the soil. The pressure propagates from the bed surface through the porous bed with a delay. The phase lag is the delay of the pressure wave normalized with the frequency. The theory of Yamamoto et al. (1978) is widely used to model the pressure propagation through a porous bed by the mentioned authors below. Raubenheimer et al. (1998) applied the theory of Yamamoto et al. (1978) to determine the wave heights based on the pressure measurements on different depths in the surf and swash zone of a fine sandy beach. The mean water depths in the surf zone are approximately 3.5 m and in the swash zone 0.3 m. Only two pressure sensors are buried in the swash zone with the upper pressure sensor ranging on a depth of 4-32 cm and the other one 97 cm below during the beach survey. The findings indicate an exponential pressure amplitude decay with small phase lags and suggest that the wave height could be determined even when the soil parameters are unknown. Pedrozo-acuña et al. (2008) observed high attenuation rates on a steep gravel beach due to a high permeability of 0.01 m/s. No phase lag observations were included in this study. Guest and Hay (2017) observed the pressure propagation on a megatidal, mixed sand-gravel-cobble beach showing good agreement with the exponential amplitude decay theory of Yamamoto et al. (1978).

The analytical solution from Yamamoto et al. (1978) for the pressure propagating through an infinitely deep porous sea bed with amplitude damping of an oscillatory component of pore pressure, is described by

$$\frac{p(z)}{p_0} = \left[1 - \frac{im\omega''}{-\tilde{k}'' + i(1+m)\omega''}\right] \exp(-\tilde{k}z) + \frac{im\omega''}{-\tilde{k}'' + i(1+m)\omega''} \exp\left(-\tilde{k}'z\right), \tag{2.9}$$

where ω and $\tilde{k}$ are the radian frequency and the wave number of the surface gravity waves in the overlying fluid, respectively. This satisfies the dispersion relation $\omega^2 = g\tilde{k}\tanh(\tilde{k}h)$. $\omega = \frac{2\pi}{T}$ and $\tilde{k} = \frac{2\pi}{\lambda}$. In case of shallow water, the wave length could be described by $\lambda = T\sqrt{gh}$. Parameters m, ω', $\tilde{k}'$ $\tilde{k}''$ are functions of the physical characteristics of the soil. $z = 0$ at the bed surface and is positive when directed into the soil. The model is based on the consolidation theory of Biot (1941). The assumption is made that the soil skeleton has linear and isotropic properties represented in Hooke's law. The flow through the soil is assumed to obey Darcy's law. The balancing between the two terms in Equation (2.9) is determined by parameter m, which includes the stiffness of the soil. For fully saturated soils, m approaches zero and only the exponential part of the first term remains. This results in an exponential pressure amplitude decay, depending on the frequency and the depth only. Another case is when the stiffness of the soil is much larger than the stiffness of the pore fluid. The first term in Equation (2.9) will approach zero and the exponential part of the second term remains. This is the case for partially saturated soils characterized in the swash zone. The analytical solution for the pressure propagation for partly saturated soils is presented by Yamamoto et al. (1978), described by

$$p = \exp\left(-k'z\right) p_0 \exp[i(kx + \omega t)]. \tag{2.10}$$

The exponential pressure amplitude attenuation and phase lag depend on the wave number (k) and the wave number prime (k'). The wave number prime is the relation between the wave number, the radian frequency (ω) and parameter a, given by

$$k' = k\left\{1 + \frac{i\omega a}{k^2}\right\}^{1/2}. \tag{2.11}$$

The wave number prime increases for a larger value of a. Not only the wave frequency determines the attenuation rate and phase lag, but also the soil characteristics are of importance. The parameter a scales the phase lag and attenuation rate based on the physical characteristics of the soil, given by

$$a = \frac{\gamma}{k_c}\left[\frac{n}{K'} + \frac{1-2\nu}{2(1-\nu)G}\right], \tag{2.12}$$

where $k_c(m/s)$ is the hydraulic conductivity, $\gamma(N)$ the weight of sea water, $n(-)$ the porosity, $K'(Pa)$ the bulk modulus, $\nu(-)$ the Poisson's ratio and $G(Pa)$ the shear modulus. The bulk modulus depends on the saturation's degree of the soil and the pressure at the boundary condition, given by

$$\frac{1}{K'} = \frac{1}{K} + \frac{1-S_r}{P_0}. \tag{2.13}$$

A saturation degree of 1 indicates a fully saturated soil without air trapped in the pores. The shear modulus depends on the Young's modulus $E(Pa)$ and the Poisson's ratio, given by

$$G = \frac{E}{2(1+\nu)}. \tag{2.14}$$

2.5 Implication on sediment transport

The pressure gradient influences two main processes: the effective sediment weight change and infiltration/exfiltration associated with the pressure gradient will change the bed shear stress.

The direction and magnitude of the pressure gradient determine the downwards and upwards directed push of the sediment, increasing or decreasing the effective sediment weight. When the effective sediment weight increases, a bigger force is needed to move the sediment, making the particle less likely to erode. The opposite happens for a decrease in effective sediment weight, resulting in a higher erosion potential.

The second process is the effect of the pressure gradient on the ventilated boundary layer. The seepage proportional to the pressure gradient changes the boundary layer at the bed surface due to infiltration and exfiltration. Exfiltration will destabilize the flow at the bed resulting in a smaller bed shear stress, while infiltration stabilizes the flow near the bed increasing the bed shear stress. This effect is displayed in Figure 2.3, which shows the flow velocity profile (u) for infiltration and exfiltration. The flow velocity near the bed is higher during infiltration causing a higher bed shear stress (τ). In contrary, the flow velocity near the bed during exfiltration is lower causing a lower bed shear stress.

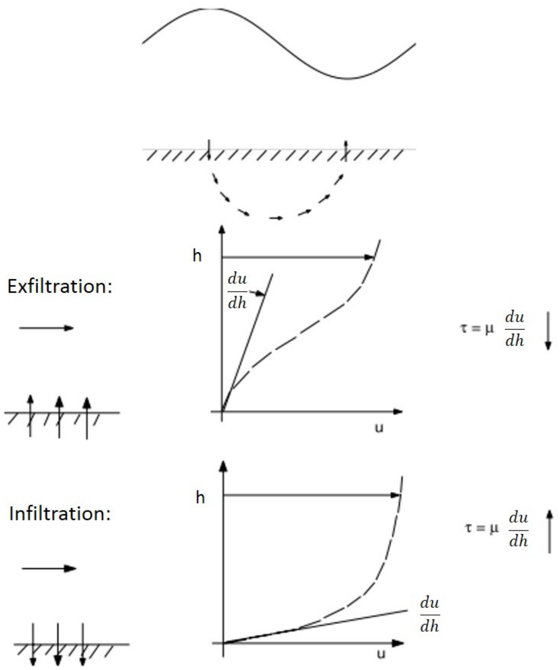

Figure 2.3: Ventilated boundary layer effect.

Conley and Inman (1994) and Lohmann et al. (2006) studied the effect of the ventilated boundary layer on the bed shear stress and the friction parameter for multiple ventilation rates. The ventilation rate is the maximum seepage divided by the maximum flow velocity. Lohmann et al. (2006) distinguished the acceleration stage, associated with the phase values of 0-90 degrees and 180-270 degrees for which infiltration occurs and the deceleration stage 90-180 degrees and 270-360 degrees for which exfiltration occurs. A bed shear stress decrease of 20% during exfiltration compared to the undisturbed case is found.

2.5.1 Modified Shields methods

Finally, multiple methods are suggested in previous studies to incorporate the change in effective sediment weight and/or the ventilated boundary layer effect. The modified Shields equations of Nielsen et al. (2001) and Francalanci et al. (2008) are used to quantify the effect of the pressure gradient on the sediment transport. Nielsen et al. (2001) proposed a method to determine the Shields number (θ) for the infiltration effect incorporating the effective sediment weight and the ventilated boundary layer studied by Conley and Inman (1994). The method is described by

$$\theta = \frac{u_{*0}^2 \left(1 - \alpha \frac{v_s}{u_{*0}}\right)}{g D_{50} \left(s - 1 - \beta \frac{v_s}{K}\right)}, \tag{2.15}$$

where $u_{*0}(m/s)$ is the shear velocity, $v_s(m/s)$ is the seepage velocity, $D_{50}(m)$ is the medium grain size, $K(m/s)$ is the permeability and $s(-)$ is the specific sediment weight. The shear velocity could be determined by multiplying the velocity by the friction factor and the water density (2.6). Parameter α and β are dimensionless coefficients given by the strength of the bed shear stress increase and the downwards drag. Nielsen et al. (2001) determined the parameter values from previous studies. $\alpha = 16$ is determined from the normalized maximum and minimum bed shear stress plotted against the ventilation parameter (Conley and Inman, 1994). $\beta = 0.35 - 0.4$ is determined from slope failure experiments (Martin and Aral, 1971).

Another method is proposed by Francalanci et al. (2008), only including the effective sediment weight forced by the seepage, given by

$$\theta = \frac{\rho u_*'^2}{\left[\rho_s - \rho \left(1 + \frac{v_s}{K}\right)\right] g D_{50}}, \tag{2.16}$$

where ρ_s and ρ are the density of the sediment and water, respectively. A comparable modification is suggested by Sumer et al. (2011) under plunging solitary and regular wave conditions, however no further research is conducted by Sumer et al. (2011) (Sumer et al., 2013). Upwards directed seepage (positive v_s) will result in a lower denominator causing a larger shields number for both Equations (2.15) (2.16). A larger Shields number indicates a higher potential for sediment transport. In case of infiltration (negative v_s) the denominator will increase, resulting in a lower Shields number. For a certain seepage, the effective weight of the sediment becomes zero. Exceeding this threshold will change the solid state of the sediment into a fluid state. In that case, the Shields number is no longer applicable.

Chapter 3

Methods

In this chapter, the methods proposed for this research are described. Figure 3.1 shows a conceptual model of the research. The first step consists of data collection to analyse the swash zone processes. Afterwards, the data from the wave flume experiments is processed and are analysed. Next, a modelling approach is suggested based on the theory of Yamamoto et al. (1978) to simulate the pressure behaviour in the soil. The model is calibrated based on the observed pressure propagation from the experiment and used to determine the pressure gradients near the bed surface. Finally, existing methods incorporating pressure gradients are evaluated based on the Shields number.

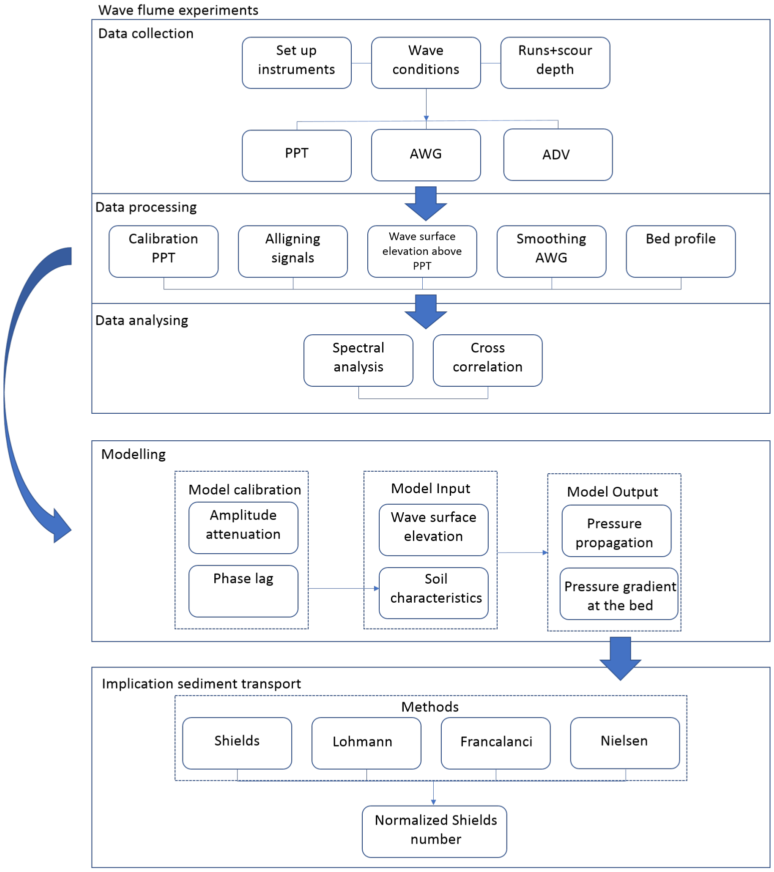

Figure 3.1: Conceptual model of the research.

3.1 Data collection

3.1.1 Experiment set up

Data was collected from wave flume experiments. The experiments were executed by the Shaping the beach Research group (van der Werf et al., 2019). The experiment set-up is described below. A large wave flume with dimensions of 100 m length, 3 m width and 4.5 m height in a facility in Barcelona is used to perform the experiments. Medium to fine sand was placed into the wave flume with a slope of 1:15, to represent a beach. The sediment size (D_{50}) is 0.25 mm, with a narrow grain size distribution (D_{10} = 0.154 mm and D_{90} = 0.372 mm), a measured settling velocity (w_s) of 0.034 m/s and a porosity of $\epsilon = 0.36$, determined in a laboratory. Three poles with pressure sensors were positioned in the swash zone (Figure 3.2. On four depths the pressure was measured in the soil during the experiment with Pore Pressure Transducers (PPT's). Bichromatic erosive waves were generated at one end of the wave flume. Acoustic Wave Gauges (AWG's) measured the water surface elevation and Acoustic Doppler Velocimeters (ADV's) measured the flow velocity. The location of the AWG, ADV (cross-shore position) and the PPT (both cross-shore position and elevation) relative to the bed with the numbering of the sensors is displayed in Figure 3.3. Table 3.1 shows the position of the PPT's.

Figure 3.2: Wave flume experiment set-up with the attached PPT and AWG on the poles (The picture is retrieved from Sara Dionisio Antonia who participated in the wave flume experiments).

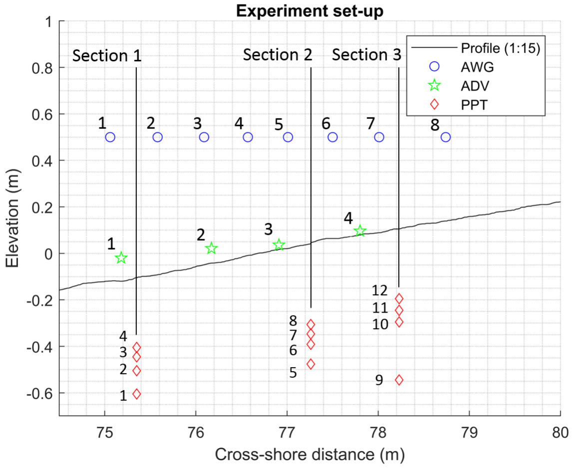

Figure 3.3: Schematization of the wave flume experiment set-up in the swash zone of the AWG, ADV and PPT instruments. The y position is relative to the mean water level (y=0).

	x-position (m)	y-position (m)
PPT 1	75.35	-0.395
PPT 2	75.35	-0.295
PPT 3	75.35	-0.235
PPT 4	75.35	-0.195
PPT 5	77.26	-0.4765
PPT 6	77.26	-0.3915
PPT 7	77.26	-0.3465
PPT 8	77.26	-0.3065
PPT 9	78.23	-0.545
PPT 10	78.23	-0.295
PPT 11	78.23	-0.245
PPT 12	78.23	-0.195

Table 3.1: PPT position.

During the experiments the bed changed but, more important for this particular research, the pressure distribution in the soil responded to the wave impact. The bathymetry after a run of 30 minutes is available with the scour depth near the poles. The AWG and PPT specifications are: ultrasonic sensors BUS005L and BUS003E with an analog output 0-10 V are used to measure the water surface elevation and pressure sensor ATM/N 24 with an output of 0-10 V were used to measure the pore pressure in the soil. The measuring frequencies of the AWG and PPT are 40 and 100 Hz, respectively.

3.1.2 Wave forcing conditions

The input parameters of the biochromatic erosive waves are displayed in Table 3.2. The wave is a composition of two main frequencies of 0.31 Hz and 0.26 Hz. The wave consists of two wave groups with 6 waves per group. The repetition period is 42 s.

$H_1(m)$	$H_2(m)$	$F_1(Hz)$	$F_2(Hz)$	$T_g(s)$	$T_r(s)$	$T_p(s)$
0.32	0.32	0.31	0.26	21.00	42.00	3.50

Table 3.2: Wave forcing input signals. H is the significant wave height, F is the frequency, T_g is the group period, T_r is the repetition period and T_p is the mean primary period.

3.1.3 Data runs

The data set consists of thirteen runs of 30 minutes of wave forcing. Before monitoring the runs, the gradually sloped bed profile is forced with random waves with a mean wave period of 4 s and a significant wave height of 0.42 m. The reason for this is to start with a beach profile which is more likely to occur in nature. Runs 1 until 4 and 9 until 13 have the wave forcing characteristics as described in the previous section. Runs 5 until 8 have one wave group instead of two with a period of 22.75 s. It is interesting to evaluate the pressure behaviour in case of a small eroded bed surface and for a large eroded bed surface. As a consequence of the lowered bed surface the PPT are closer located to the bed surface. In this study, the data from run 3 and 9 are used to determine the pressure behaviour.

The bed surface level at sections 1, 2 and 3 needs to be determined from the profile data measured after each run (Figure 3.4), including the manually measured scour depth at each pole for the specific run. This enables us to determine the depth of the PPT's relative to the bed surface level. The profile measured after the previous run is used to determine the bed surface level at the cross-shore location of the PPT's. The bed surface elevation is determined by subtracting the manually measured scour depth at the pole (Appendix B).

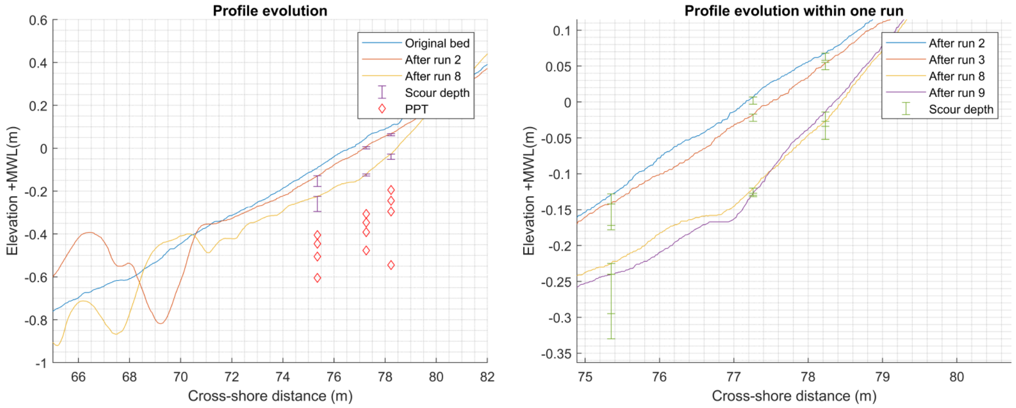

Figure 3.4: Profile evolution due to erosion and accretion changing the bed surface level and scour depth.

	Section 1	Section 2	Section 3
Run 3	1 cm	2 cm	1 cm
Run 9	3 cm	0 cm	2 cm

Table 3.3: Bed surface change within one run in order of centimeters.

The bed surface level changes during a thirty minute run. The bed profile evolution within one run is determined (Table 3.3). The largest bed erosion rate occurs during run 9 for section 1. Generally, the bed surface level changes a couple of centimeters within one run. The bed surface level already changes during a swash cycle in order of millimeters, due to erosion and accretion. van der Zanden (2016) showed bed surface level fluctuations up to 13 mm within one swash cycle. This results in an uncertainty of the bed surface elevation. A sensitivity analysis will be performed changing the bed surface elevation a couple of centimeters. This uncertainty greatly affects the referencing of the boundary condition at the bed.

3.2 Data processing

The raw data needs to be processed to be usable for the data analysis. The data set consists of thirteen runs of 30 minutes of which two runs are used. One in the beginning (third run) and one near the end (ninth run) of the experiment to incorporate a run with a little erosion and one with a lot of erosion at the three sections. Appendix A shows the processed data.

Calibration of the PPT

PPT's convert an applied pressure into a linear and proportional electrical signal (Voltage), which needs to be converted to Pascal. The mean constant water level (z_{MWL}) is known with the corresponding electric signal in voltage when no waves are forced in the system. The depth of each sensor is known (z_{ppt}), so for each sensor the water column above could be determined. Next, the pressure in pascal could be computed for the mean water level (3.1).

$$P = \rho g (z_{MWL} - z_{PPT}) \tag{3.1}$$

Aligning the PPT and AWG signals

When the experiment starts (t=0 for the AWG), there is a delay till the paddle start moving and the AWG starts recording. When the paddle starts a synchronizing signal is send to the AWG to start recording. At the same moment the PPT is set to t=0. The flow chart is displayed in Figure 3.5. The lag needs to be subtracted from the time vector for the AWG in order to align both signals. The exact lag needs to be determined, because it differs for each run. The first value of the time vector for a run is subtracted in order to align both signals.

Wave surface elevation at the equal cross-shore position of the PPT

The cross-shore position of the AWG does not match the PPT position exactly. Therefore, the water surface elevation at the same position as the three sections of the PPT needs to be determined. A cross covariance analysis is performed in order to determine the lag between the AWG's. The three PPT sections are located between AWG 1 and 2, AWG 5 and 6 and AWG 7 and 8, respectively (Table 3.4). The lag between these AWG is determined for both runs, assuming a linear cross shore propagation velocity. The propagation velocity is compared to the propagation velocity for shallow water $c = \sqrt{gh}$ with a water depth in between 0.3-0.4 m. This results in propagation velocities of 1.7-2.0 m/s, comparable to the observed wave propagation velocities displayed in 3.4.

	AWG 1	PPT	AWG 2	AWG 5	PPT	AWG 6	AWG 7	PPT	AWG 8
x-position (m)	75.06	75.35	75.58	77.01	77.26	77.50	78.01	78.23	78.74
Propagation velocity (m/s)	1.7			2.0			1.8		

Table 3.4: Cross-shore position AWG and PPT with the propagation velocity of the wave.

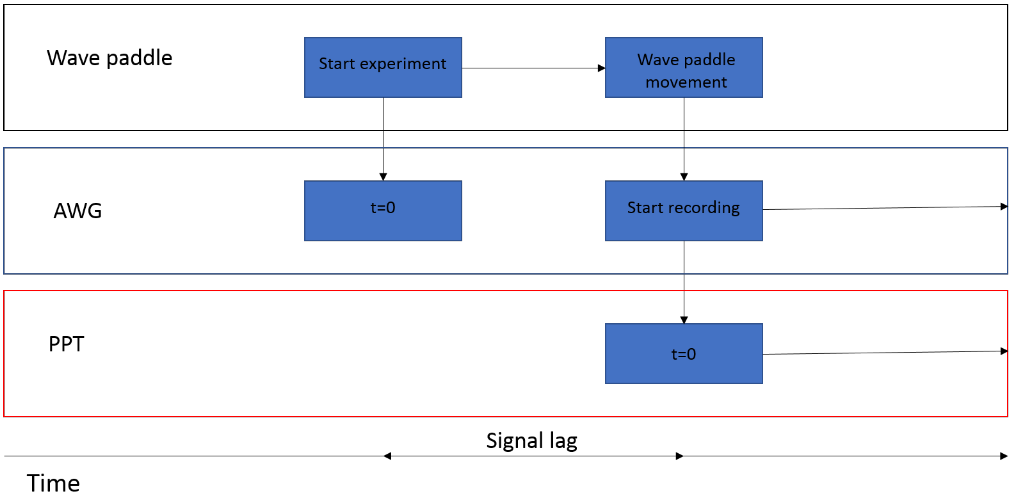

Figure 3.5: Flow chart AWG and PPT signal

Smoothing

The AWG signal needs to be smoothed, because it has a measuring noise. The smoothing window is chosen, that only these small fluctuations are extracted. The Hanning method is used to smooth the water surface elevation with a smoothing window of 16 data points, corresponding to window length of 0.4 s. There is no need to smooth the PPT signal.

3.3 Data analysing

3.3.1 Spectral analysis

A spectral analysis for both the pressure and wave surface elevation is performed to identify the frequencies in the signal. One of the purposes is to link the pressure signal frequencies to the wave forcing frequencies. Another purpose is to survey how the pressure signal propagates deeper into the bed. The energy spectra of the pressure on different depths will be compared and the phase lag between the upper pressure sensor and the lowest located pressure sensor will be identified. We expect that the frequencies of the wave could be identified in the spectral power density plot of the pressure. On top of that, higher harmonics should be considered which are multiples of the initial frequency.

A Fast Fourier Transformation (FFT) is applied to obtain the energy spectrum according with a suitable window for sinusoid signals. There are multiple types of windows which could be chosen suitable for periodic signals: Hann window, Blackmanharris window or Hamming window. Each window is evaluated and shows peaks at equal frequencies. Only the magnitude of the amplitude differs for the windows. The Hann window is used for further computations.

3.3.2 Pressure gradients

The pressure in the soil at multiple depths was observed in the wave flume. From these measurements, the vertical pressure gradient is derived. The pressure gradients in a soil layer are determined by the central difference method with the following formula:

$$\frac{\partial p}{\partial z} = \frac{p_{z1} - p_{z2}}{z_1 - z_2}, \tag{3.2}$$

where $p(Pa)$ is the pressure and $z(m)$ is the depth of the PPT. The pore pressure gradient in the middle of the soil layer is approximated at the midpoint in between the PPT's.

3.4 Pressure propagation model

The pressure propagation through the porous bed is modelled under wave forcing conditions. The model is used to estimate the pressure gradient magnitudes in the bed at different elevated soil layers. Different wave groups could be assessed to evaluate the pressure gradient response. In order to model the pressure propagation through the soil in the swash zone, assumptions needs to be formulated concerning the pressure behavior in the soil.

3.4.1 Modelling approach

A model is set up, to simulate the pressure propagation in time, by increasing depth under the forcing waves. This is done with the boundary condition set at the bed surface for the pressure P_0 at $z = 0$ which is derived from the wave surface elevation. The pressure propagation through the porous bed by increasing depth (z), in cross shore direction (x) in time (t) is described (2.10). The pressure boundary condition (P_0) depends on the wave surface elevation forcing on the bed varying in time. A situation sketch is displayed in Figure 3.6.

Input of the wave surface elevation

The water surface elevation consists of a composition of multiple frequencies, while the solution of Yamamoto et al. (1978) only incorporates one frequency (wave number k), because the pressure amplitude attenuation and phase lag rate are frequency dependent (2.10). The pressure attenuation for high frequencies is larger compared to small frequencies, which means that for each frequency the attenuation rate needs to be determined. Therefore, the smoothed wave surface elevation signal needs to be decomposed into a set of sinusoids. The composed signal of frequencies is decomposed with the Fast Fourier

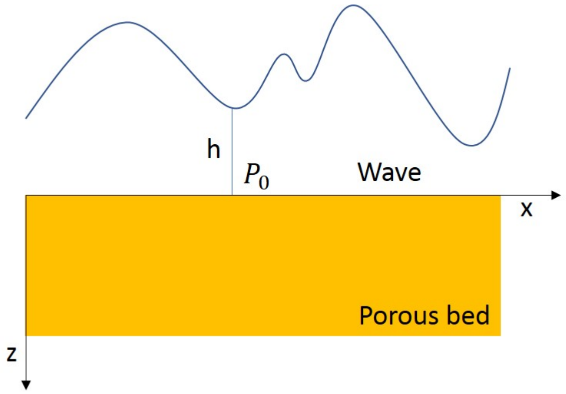

Figure 3.6: Situation sketch

Transformation in order to identify each frequency component with the corresponding magnitude and phase, resulting in a two sided spectrum. The single sided spectrum is obtained and used as an input in the model. The original signal can be described by a sum of sinusoids with a magnitude and phase coefficient. These coefficients are expressed by a complex number $(a + bi)$ for which the length of the vector is the magnitude and the angle is the phase. Summation of the complex numbers representing a set of sinusoids will result in the original signal rewritten according to Euler's law:

$$\sum_{j=1}^{J} A_j exp(i(\omega_j t + \phi_j)), \tag{3.3}$$

where A_j is the magnitude (amplitude), ϕ_j is the phase of the complex vector and J is the number of frequencies in the FFT.

For each frequency in the spectral domain of one repetition period (42 s) the stored complex number representing the magnitude and phase is used to compute the water surface elevation. The pressure P_z is computed by multiplying P_0 by the amplitude frequency plot for a certain depth z, according to the partly saturated solution of Yamamoto et al. (1978). High frequencies attenuate faster than low frequencies and an increasing depth will decrease the amplitude. In the end, a summation of pressure signals in time will result in a composed pressure signal from all frequencies. The flow chart is displayed in Figure 3.7.

Boundary condition P_0

For partly saturated soils the pressure propagation is described at depth z in time t with $x = 0$ (2.10). The boundary condition P_0 at the bed surface as a response to the wave forcing needs to be determined. The dynamic pressure variation is needed as an input in the model. When hydrostatic pressure is assumed the pressure at the bed (P_0) is described by:

$$P_0 = \rho g h + P_a, \tag{3.4}$$

with

$$h(t) = A\cos(\omega t + \phi). \tag{3.5}$$

In case of low water levels this assumption is applicable because the dynamic pressure variation in the wave surface elevation is hardly damped towards the bed surface.

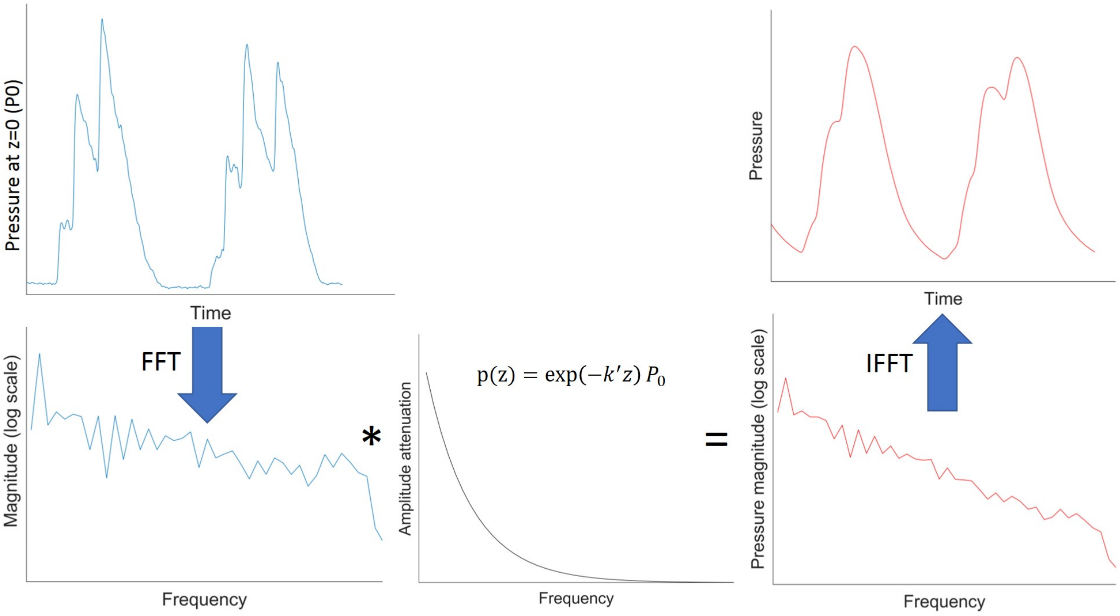

Figure 3.7: Flow chart from boundary condition pressure at z=0 (upper left) to spectral magnitude frequency plot (bottom left). Multiplied by frequency dependent exponential attenuation at depth z for each frequency described by the exponential solution of Yamamoto et al. (1978) (bottom middle) in order to obtain a set of sinusoids for all frequencies with higher attenuation rates for high frequencies (bottom right). Recomposed time series by IFFT including of all frequencies (upper right).

If the wave surface levels are larger, wave induced pressure is damped in the water column towards the bed surface, so linear wave theory should be assumed, described by

$$\mathrm{p} = -\rho \mathrm{g}\mathrm{h}_{\mathrm{ref}} + \rho \mathrm{g} A \cos(\mathrm{kx} - \omega \mathrm{t}) \frac{\cosh(\mathrm{k}(\mathrm{h}_{\mathrm{m}} + h_{ref})\}}{\cosh \mathrm{kh}_{\mathrm{m}}} + P_a, \tag{3.6}$$

where h_{ref} is the depth in the water column for which the pressure needs to be computed relative to the mean water level h_m. So, at the bed surface $h_{ref} = -h_m$. We are only interested in the boundary condition P_0 at the bed surface and the dynamic part of the linear wave equation. Therefore, the Equation is rewritten in terms of the imaginary exponent describing the wave in time:

$$\mathrm{p} = \rho \mathrm{g} A exp(i(\omega t + \phi)) \frac{1}{\cosh\,(\mathrm{kh}_{\mathrm{m}})}. \tag{3.7}$$

The difference between the hydrostatic pressure and the linear wave theory is the pressure attenuation factor in the water column, depending on the mean water level and the wave number. The linear wave theory is used to compute the pressure at the bed (P_0).

Pressure modelling

The pressure signal for each frequency (j) is computed with the partly saturated analytical solution from Yamamoto et al. (1978) for $x = 0$, because the pressure propagation at one section will be computed, rewritten with an imaginary exponential component in time describing the wave and z component to determine the amplitude attenuation rate and phase shift, without the atmospheric pressure P_0. An inverse Fast Fourier Transformation will recompose the signal, represented by a summation of the pressure signal at depth z in time:

$$p = \sum_{j=1}^{J} \exp\left(-k'_j z\right) A_j \exp\left(i(\omega_j t + \phi_j)\right) \rho g \frac{1}{\cosh\left(\mathrm{k_j h}\right)}, \tag{3.8}$$

where A_j, ϕ_j and ω_j are the amplitude, phase and radian frequency obtained from the decomposed wave surface elevation, respectively. ρ is the sea water density and g is the gravitational acceleration. k'_j is the phase shift and attenuation rate (2.11), scaled with parameter a.

3.4.2 Model calibration

The model is calibrated based on the observed pressure attenuation from the wave flume experiment. Sections 1, 2 and 3 for run 3 and 9 are used to calibrate the model. The soil characteristics are captured in parameter a (2.12). The bulk modulus of the saturated water in the soil (dependent on the saturation degree (2.13)), the hydraulic conductivity, weight of the sea water, Poisson's ratio, Young's modulus and porosity are included in parameter a. These soil parameters are uncertain and needs to be calibrated. Only parameter a will be calibrated, because all soil characteristics are represented in this parameter.

A cross covariance analysis is performed identifying the lag for which the modelled data fits the best to the experiment data. Also the correlation parameter between the modelled and observed pressure, ranging from 0-1, will be determined. Approaching 1 will indicate a high correlation degree. The sampling rate of the modelled data and the experiment data should be equal in order to compute the correlation degree. It is not time efficient to increase the number of data points in the time interval in the model, because this will increase the computation time of the model. Therefore, the modelled data with a time interval of $0.1s$ is upsampled to a frequency of 100 Hz to $0.01s$.

Two methods are chosen to indicate the correlation between the observed and modelled pressure: the Root Mean Square Error (RMSE):

$$\mathrm{RMSE} = \left[\sum_{n=1}^{N} \left(P_o(n) - P_m(n)\right)^2 / N\right]^{1/2}, \tag{3.9}$$

where P_o and P_m are the observed pressure data from the experiment and the modelled pressure, respectively, normalized with the standard deviation of the observed pressure (σ), described by

$$\sigma = \sqrt{\frac{1}{N} \sum_{n=1}^{N} \left(P_o(n) - \mu\right)^2}, \tag{3.10}$$

where μ is the mean pressure and the Nash Sutcliffe model efficiency coefficient (NS), given by

$$NS = 1 - \frac{\sum_{n=1}^{N} \left[P_m(n) - P_o(n)\right]^2}{\sum_{n=1}^{N} \left[P_o(n) - \overline{P_o}\right]^2}. \tag{3.11}$$

The first method gives a quantitative error for the modelled pressure normalized with the standard deviation to compare the error at multiple depths. The pressure amplitude at a deeper depth is smaller in comparison to a smaller depth, so the quantitative error will also be smaller. A normalization with the standard deviation for each depth will enable to compare the error with different depths. The second method, qualitatively describes the correlation between the modelled and observed pressure.

A root mean square error of 0 indicates a perfect fit. Positive errors represent the time averaged squared deviation. The Nash Sutcliffe effciency ranges from $-\infty$ to 1. A NS of 1 indicates a perfect fit. The model is calibrated on the above mentioned accuracy of fit parameters.

3.4.3 Pressure gradient computation for the model

In contrast to the experimental pressure gradient determination, the modelled pressure gradient not necessarily has to be approximated by the central difference method, but is computed analytically. This is far more accurate than approaching the pressure gradient in the midpoint of a soil layer with a thickness up to 25 cm. The pressure gradient computation in a point is possible, because the pressure attenuation and phase lag in z is computed, according to a formula (2.10). Therefore, the derivative in the z could be computed from the formula. The first derivative in z represents the pressure gradient, described by

$$\frac{\partial p}{\partial z} = -k' \exp(-k'z) p_0 \exp[i(kx - \omega t)]. \tag{3.12}$$

The pressure gradient at the bed surface is obtained by evaluating the pressure at $z = 0$, given by

$$\frac{\partial p}{\partial z}|_{z=0} = -k' p_0 \exp[i(kx - \omega t)]. \tag{3.13}$$

3.5 Modified Shields formulations

Several studies, mentioned in the Theoretical background section, are conducted to incorporate the influence of the pressure gradient on the effective sediment weight and the ventilated boundary layer due to infiltration and exfiltration. In order to study the implication of the pressure gradient on sediment transport the dimensionless bed shear stress is determined. The methods of Nielsen et al. (2001) (2.15) and Francalanci et al. (2008) (2.16) are used to compare the pressure gradient induced effects on the Shields number. The Shields number describes the dimensionless bed shear stress and is a well known indicator for sediment transport. A higher Shields number will indicate an increased probability of sediment transport.

The pressure gradient, permeability, bed shear stress, density and medium grain size are needed to determine the Shields number according to the proposed methods. The pressure gradients at the bed surface computed by the model are used.

Due to the high uncertainty in permeability two methods are used to set a range of realistic permeability values. The permeability is determined from Hazen (2.3) and Kozeny-Carman (2.4). The permeability ranges in between both determined values. $D_{10} = 0.154mm$ and the porosity $\epsilon = 0.36$. When $A = 1.5$ the permeability is $3.6 * 10^{-4} m/s$. This would be the highest possible permeability according to this method. Kozeny-Carman equation with a viscosity of $1 * 10^{-4} m^2/s$ for water at 20 degrees gives a permeability of $1.5 * 10^{-5} m/s$. Both methods differ one order from each other, restating the high uncertainty in the permeability. The permeability in the range from $1.5 * 10^{-5} - 3.6 * 10^{-4} m/s$ is evaluated in the Shields parametrizations.

The bed shear stress will be computed with the formulation of Reniers et al. (2013) with a Chezy coefficient of $65 m/s^{1/2}$, representative of waves breaking on a planar beach (2.6) (2.7). This corresponds to a friction parameter c_f of 0.0023. The bed shear stress is determined based on the flow velocity at the bed. The velocity is measured by the ADV at a certain vertical distance to the bed. An uniform velocity profile is assumed, so the velocity at the bed is assumed equal to the measured velocity. ADV 3 and 4 are the nearest cross-shore located to the PPT's with a cross-shore position of 76.91 m and 77.80 m, respectively. The velocity profile for a wave period (42 s) is used to evaluate the Shields number during both uprush and backwash, revealing the highest magnitudes during one wave period as well. The model is interpolated from 10 Hz to 100 Hz to have an equal number of data points for the pressure gradients and the measuring frequency of the ADV. The ADV is unable to cope with very small water levels or no inundation, resulting in a fluctuating velocity signal. In this case, the velocity is assumed to be zero because there is no flow.

All input parameters needed to compute the normalized Shields number are discussed. An analysis is performed to weight the effect of the effective weight of the sediment and the ventilated boundary layer on the Shields number, based on the methods. First, the Shields number without the effective weight of the sediment and ventilated boundary effects is determined. Afterwards, both the individual effect of these processes is assessed and combined in the end.

Chapter 4

Results

In this chapter the results of the research are presented. First, the outcomes of the analyzed wave flume experiment data is outlined. Second, the model calibration values are reported and the modelled pressure gradients at the bed surface are presented. Finally, the outcomes of the influence of the pressure gradients on different modified Shields parametrizations are presented.

4.1 Wave flume experiment observations

The observed wave surface elevation and pressure behaviour is analysed. The relation between the wave surface elevation and the pressure at multiple depths is studied by using a spectral analysis.

4.1.1 Wave forcing characteristics

The wave surface elevation for the three sections over a period of four swash cycles is plotted in Figure 4.1.

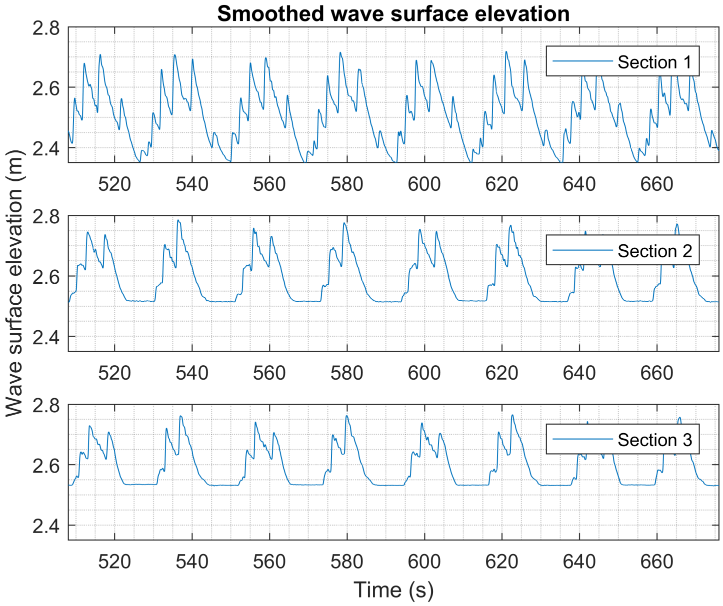

Figure 4.1: Smoothed wave surface elevation for sections 1, 2 and 3

The duration of one swash cycle is 42 seconds (T_r). The wave height reduces shorewards decelerated by the bed friction and bed slope. The significant target wave height of 0.65 m is reduced to 0.4, 0.3 and 0.25 m for section 1, 2 and 3, respectively. The generated six waves per group are still recognizable for the most offshore section 1. For section 2 and 3, the six waves per group are merged to two/three waves per group and there are periods of no inundation with a duration up to 8 s.

4.1.2 Pressure distribution

The PPT's are calibrated according to the linear fit functions (Appendix A). The dynamic pressure is obtained by excluding the hydrostatic pressure, wave set up and residual pore pressure build-up effects. The hydrostatic pressure is computed by

$$static\ pressure = \rho g h, \tag{4.1}$$

where $\rho = 1000 kg/m^3$, $g = 9.81 m/s^2$ and h is the vertical distance of the PPT relative to the MWL of 2.47 m. Wave set up will increase the water level relative to the MWL at the onshore sections. These effects equally influence the pressure at different depths. Besides that, the mean pressure increases depth dependently at the beginning of a run, possibly caused by the physical process, residual pore pressure build-up. The rearrangement of the sediment grains will move relative to each other and change the pore volume. A pore pressure change occurs when the drainage velocity is smaller than the rate of volume change. This could lead to residual liquefaction (Sumer, 2014). In order to compare the pressure signals at different depths, the mean at each depth needs to be subtracted to cope with all processes mentioned above. The dynamic pore pressure is plotted in Figure 4.2 for each section.

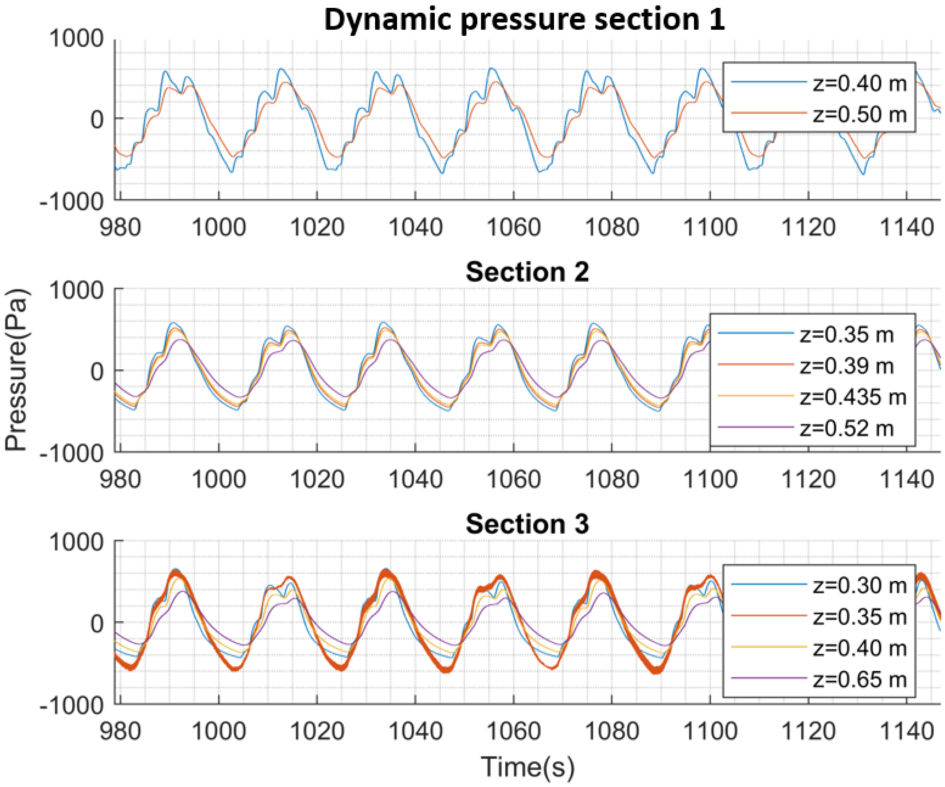

Figure 4.2: Pressure distribution for three sections on different depths (run 3).

During previous experiments, with an equal experiment set up for erosive waves with four waves per group, scour near the pole of section 1 exposed the upper two PPT's after a couple of runs. Therefore, PPT 3 and 4 were removed, so there are only two pressure measurements depths at section 1. Furthermore, PPT 11 shows a noisy signal, caused by the small range in the Voltage signal of this PPT (0.51-0.57 V), resulting in a lower accuracy than the other PPT's. For that reason also PPT 11 is not used in further analysis. In between depth 0.39 m (red line) to 0.435 m (yellow line) for section 2 a small pressure amplitude attenuation is visible, compared to the attenuation from 0.35 m (blue line) to 0.39 m. The distance in between these three PPT's is almost equal (4 cm and 4.5 cm). Therefore, we would expect a pressure amplitude attenuation of the same order. From Figure 4.2 it can be seen that the pressure amplitude peaks decrease by increasing depth. An exponential decay of the pressure amplitudes is suggested by Yamamoto et al. (1978).

4.1.3 Spectral analysis

The spectrum of the wave surface elevation is compared to the pressure sensor closest to the bed surface at section 1 (z=0.40 m) and 2 (z=0.35 m) (Figure 4.3). Bichromatic waves were generated containing two frequencies: 0.26 Hz and 0.31 Hz. The peaks of the wave surface elevation from section 1 are larger than section 2. This means that energy is lost when the wave approaches shorewards. Furthermore, the wave surface elevation and pressure spectra show peaks at the same frequencies meaning that the pressure responses to the wave forcing. Table 4.1 shows a selection of the largest peaks with the origin of the frequency.

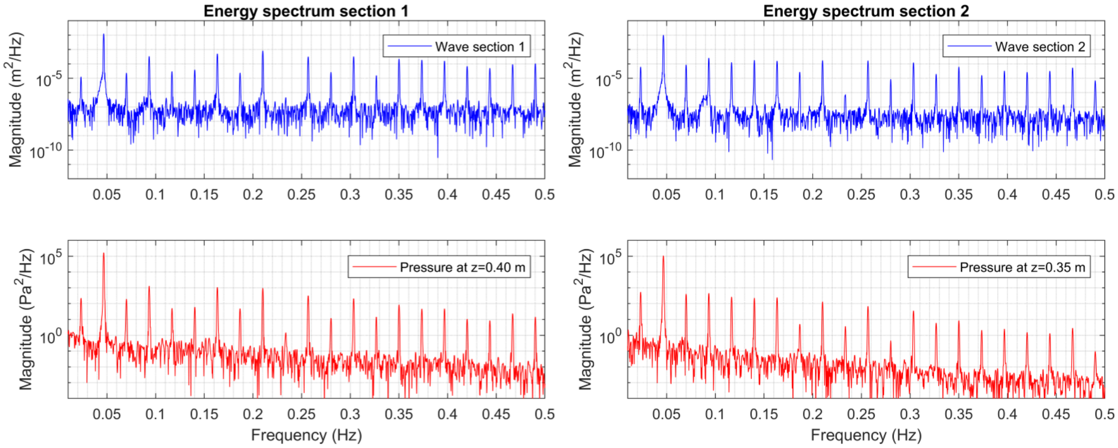

Figure 4.3: Energy spectrum wave surface elevation and pressure (PPT 8) at section 2

Energy peaks	Frequency (Hz)	Period (s)	Origin of the peak
1	0.02	42	T_r
2	0.05	21	T_g
3	0.07-0.21	-	Higher harmonics T_g and T_r
4	0.26	3.8	$f_2(t) = H_2 \sin(0.53\pi t)$
5	0.28	3.5	T_p
6	0.30	3.3	$f_1(t) = H_1 \sin(0.62\pi t)$

Table 4.1: Dominant energy peaks. T_r is the repetition period, T_g is the group period and T_p is the mean primary period. H is the significant wave height

The Energy spectrum for multiple depths for section 2 is displayed in Figure 4.4. At multiple frequencies, peaks in the energy spectrum occur. The magnitude of the peaks decrease by increasing depth.

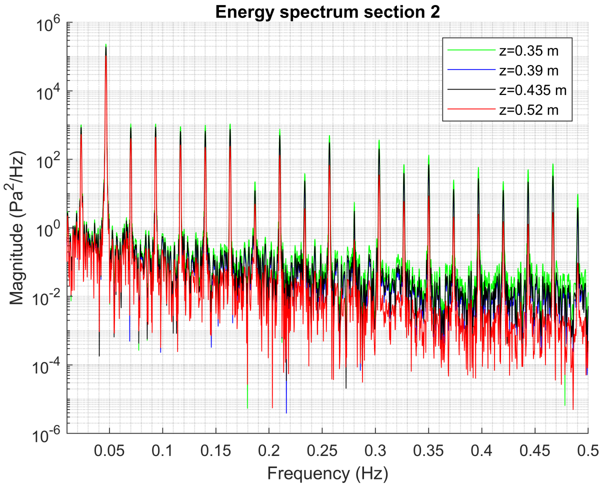

Figure 4.4: Energy spectrum pressure at multiple depths at section 2

Phase lag

The pressure propagates with a certain velocity through the soil, which depends on the stiffness of the porous medium and the frequency. The frequency dependent phase lag is examined with a spectral analysis. The phase lag in degrees for frequencies in the range of 0 to 0.5 Hz are determined. The phase lag between the upper PPT and the deepest PPT could be determined by subtracting the phase of one another. The phase lag in the range of 0-0.5 Hz for section 1, 2 and 3 is displayed in Figure 4.5. The phase lag is frequency dependent and section 3 shows a larger phase lag than section 1 and 2. This is explained by the larger distance in between the upper and lower PPT for section 3 in comparison to section 1 and 2, 35 cm, 10 cm and 17 cm respectively.

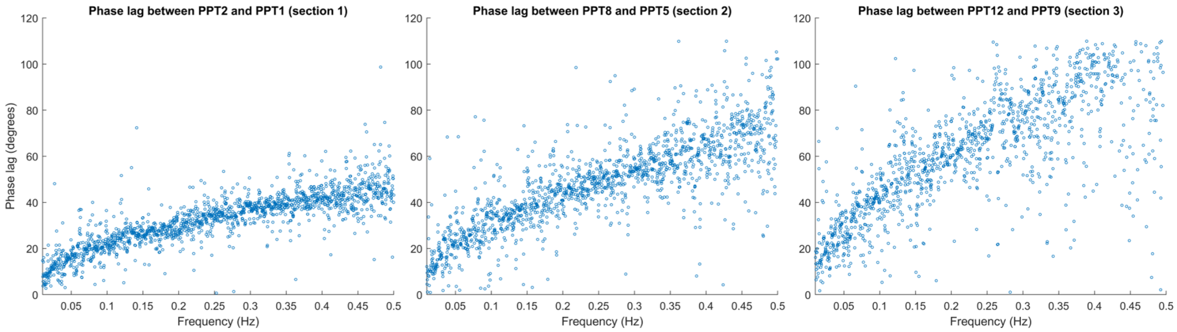

Figure 4.5: Phase lag between PPT 2 (z=0.30 m) and PPT 1 (z=0.40 m), section 1. Phase lag between PPT 8 (z=0.35 m) and PPT 5 (z=0.52 m), section 2. Phase lag between PPT 12 (z=0.30 m) and PPT 9 (z=0.65 m), section 3.

The phase lag could also be expressed in terms of time in order to compare the delay for different frequencies, given by

$$Phase\ lag(s) = \frac{\theta_{degrees}}{360F}, \tag{4.2}$$

where θ is the phase lag (degrees) and F is the frequency (Hz). First, a scatter density plot of the phase lag between the PPT's is derived (Figure 4.6). The probability density estimate scatter plot is applied with a Kernel smoothing function. The Kernel smoothing function is a statistical technique to estimate the density of data with a certain reach, by weighting the neighboring observed data. A range from 0-110 degrees is set for the phase lag in order to eliminate 360 degrees shifted phase lags. A trend line is fitted for each density scatter plot to address the phase lag expressed in the frequency in terms of a function. The equations for the fitted polynomials are described in the Appendix A.

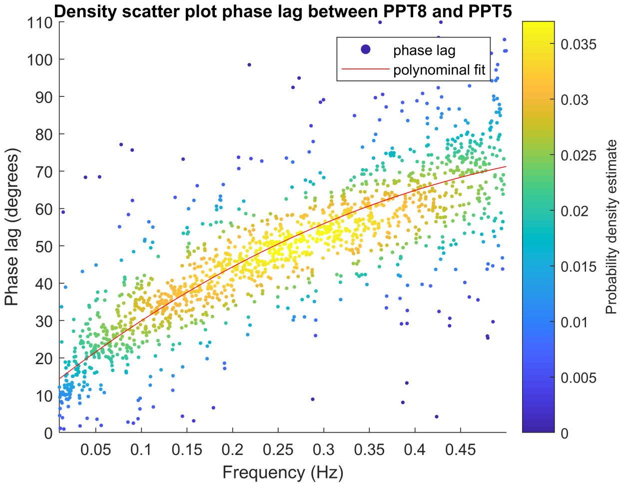

Figure 4.6: Density scatter plot with a fitted polynomial between PPT 8 and 5 of section 2.

The phase lag for different frequencies is determined with the fitted equations. The frequency dependent delay in time is displayed in Figure 4.7 (4.2). Section 1 and 3 only have pressure measurements at two and three different depths, respectively. Therefore, only section 2 is evaluated. The phase lag for the dominant frequencies from the spectral analysis are compared at different depths. The low frequencies show a larger delay compared to the high frequencies. For an individual frequency a linear relation is visible between the phase lag and the depth. The pressure propagation velocity for 0.26 and 0.31 Hz are approximately 0.4 m/s. The pressure propagation velocity for a wave group of 0.05 Hz is approximately 0.1 m/s.

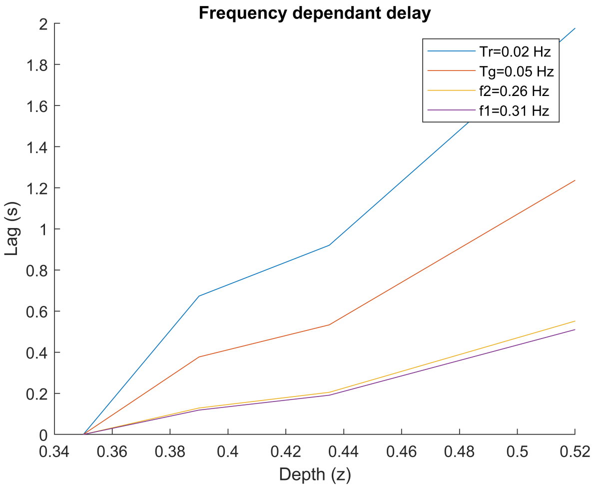

Figure 4.7: Frequency dependent delay for section 2.

4.2 Vertical pressure gradients

The pressure gradients in between the PPT's are determined for the 3 sections. The pressure gradient is computed with the central difference method for multiple soil layers in between the midpoint of the PPT's (3.2). The pressure gradient is aligned in time with the wave surface elevation for the three sections (Figure 4.8, Figure 4.9 and Figure 4.10).

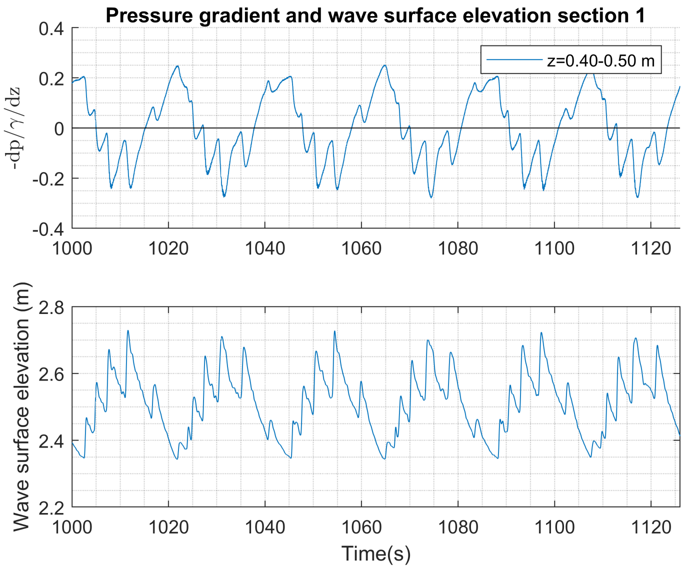

Figure 4.8: Pressure gradient and smoothed water surface level section 1. When $-\frac{\partial p}{\partial z} > 0$, there is an upwards directed pressure gradient force on the sediment indicating exfiltration.

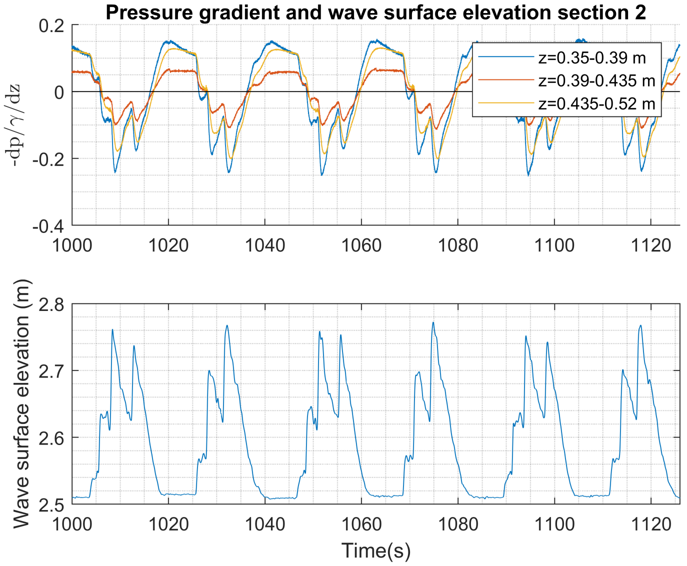

Figure 4.9: Pressure gradient and smoothed water surface level section 2.

When $-\frac{\partial p}{\partial z} > 0$, there is an upwards directed pressure gradient force on the sediment indicating

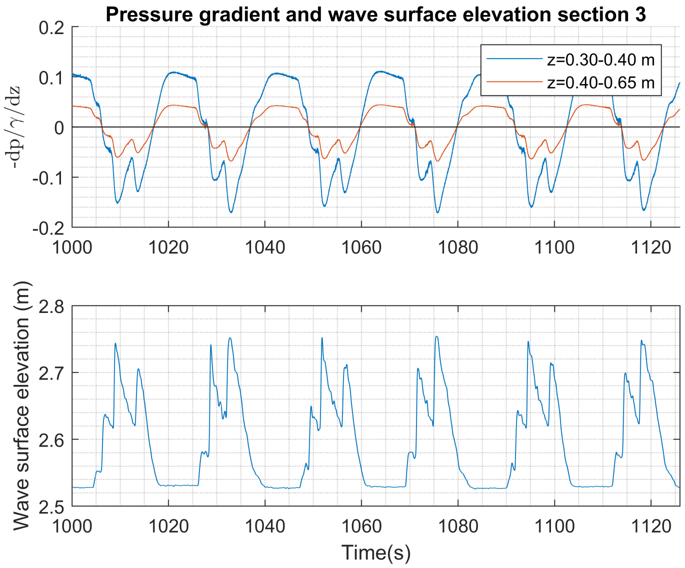

Figure 4.10: Pressure gradient and smoothed water surface level section 3.

exfiltration. The physical process is described as follows: the water height above the bed increases, when a wave approaches the shore. The weight of the water column pushes water through the porous bed infiltrating in the soil. An increase in the water height will increases the force on the bed resulting in a higher infiltration rate. The infiltration is linearly related to the pressure gradient, according to Darcy's law (2.2). The negative pressure gradient is the highest for large wave heights and decreases if the water height reduces. When the water levels are low, water trapped in the pores in the sediment exfiltrates, associated with a positive pressure gradient. The weight of the water from the next wave group will shift the exfiltration process to infiltration, towards a negative pressure gradient. The magnitude of the pressure gradients decreases by increasing depth as a consequence of the pressure amplitude attenuation.

For high surface elevations a downwards directed pressure gradient forces on the soil indicating infiltration. For section 2, the pressure gradient does not behave as we intuitively would expect. Due to the exponential pressure amplitude decay and linear phase lag we would expect an decrease in pressure gradient magnitude for increasing depth. However, the pressure gradient in between 0.39-0.435 m (red line) is smaller than for 0.435-0.52 m (yellow line) (Figure 4.9). As a result of the observed small pressure amplitude attenuation in between the PPT's at 0.39 m and 0.435 m, described in the previous section. This error might be the result of an inaccuracy in the distance between the two pressure sensors. If the pressure sensors appear to be closer positioned than assumed, the magnitude of the pressure gradient would be smaller (3.2).

For sections 2 and 3, the duration of the upwards directed pressure gradient in the upper soil layer is larger than the downwards directed pressure gradient. This is caused by the periods of no inundation and small water depths leading to exfiltration. In between two wave groups, the maximum $-\frac{\partial p}{\partial z}$ is reached just before another wave group approaches. In case of random waves, the duration between two wave groups might influence the maximum pressure gradient. A longer and shorter duration in between the wave groups will increase and decrease the maximum pressure gradient, respectively. The pressure gradients in the soil near the bed surface is the most interesting, concerning sediment transport, because the waves will force the sediment at the bed surface. The depth of the PPT's is too large to estimate the pressure gradient in the upper soil layer. Therefore, the pressure propagation will be modelled, which enables us to determine the pressure gradient near the bed surface. At deeper depths the magnitude of the pore pressure gradient decreases which is the result of the exponential pressure amplitude attenuation. The pressure gradients for the three sections show that the maximum $-\frac{\partial p}{\partial z}$ decreases shorewards (from section

1 to section 3), as a result of the decrease in wave surface elevation. Despite that, the upper PPT for each section has a different burial depth and scour depth, depending on the run. The pressure gradients are closely linked to infiltration/exfiltration and obey Darcy's law (2.2). A pore pressure gradient indicates the flow within the soil layer.

4.3 Modelled pressure propagation

The pressure propagation is modelled and calibrated from the observed pressure in the wave flume. The model is used to compute the pressure gradients at the bed surface.

4.3.1 Boundary condition and forcing parameters

The boundary condition at the bed surface is harmonically forced by the wave surface elevation. Figure 4.11 shows the wave surface elevation and the pressure signal at $z = 0$ for section 1 and section 2 (3.7). The pressure boundary condition at $z = 0$ is nearly linear related to the wave surface elevation, because the damping factor from the linear wave theory approximates 1 for dominant frequencies at small water depths (h). In a FFT analysis, the mean is used as a reference (water level is zero) with positive and negative water levels. This will also result in negative pressures for the boundary condition. A vertical translation of the mean will restore this, such that only a positive pressure can occur. For dry periods, the pressure is zero. This is clearly visible for section 2.

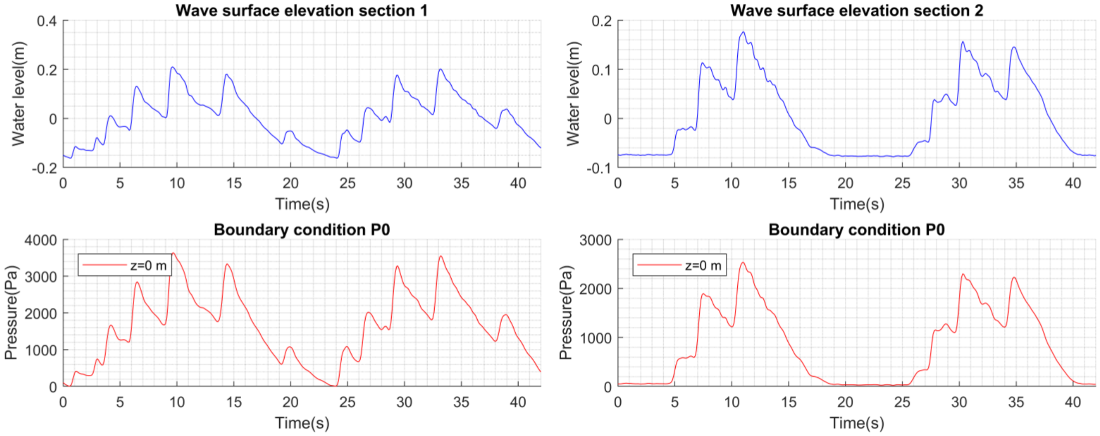

Figure 4.11: Wave surface elevation and boundary condition P_0 for section 2.

4.3.2 Model calibration

The model is calibrated based on the methods presented in the Methodology Chapter. All three sections are calibrated for two different runs individually. Local conditions, like the permeability and saturation degree may result in a different calibration parameter. From run to run, wave forcing can lead to local sediment sorting and bed level changes. The permeability for finer sediment particles is lower than for coarser sediment particles. Also, bed level changes change the saturation degree in the soil. The third run has a small bed erosion and the ninth run shows a more eroded bed. Hence, sediment sorting locally changes the permeability and bed level change affects the saturation degree. Therefore, each section is calibrated individually for two runs. Parameter a, including the soil characteristics, is calibrated. First, a parameter for a is chosen such that the model visually fits the data. Afterwards, a range of $a = 30 - 40$ is chosen to determine the best fit. The accuracy of fit in the range is determined by the methods for which the outcomes are presented in Appendix B. Figure 4.12 shows the modelled dynamic pressure at three depths with the RMSE indicated by the shaded area for section 3. The bed level in comparison to the original 1:15 sloped bed, shows a lowering due to erosion after run 2 of 0.087, 0.053 and 0.042 m for section 1, 2 and 3, respectively (Appendix B). After run 8, a lowering of 0.204, 0.154 and 0.157 m is present for section 2 and 3, respectively. The depth of the PPT's are lowered by these erosion depths. The calibration criteria for the normalized RMSE and Nash Sutcliffe for different values for parameter a are given in Appendix B. The calibrated a values for the sections for run 3 and 9 are displayed in Table 4.2. The values for parameter a ranges from 30-37.5. For run 3 the parameter a value is a little lower than for sections 1 and 2. Run 9 shows comparable values for a.

	Section 1	Section 2	Section 3
Run 3	a=37.5	a=37.5	a=32.5
Run 9	a=30	a=32.5	a=32.5

Table 4.2: Calibrated a value for each section for run 3 and 9.

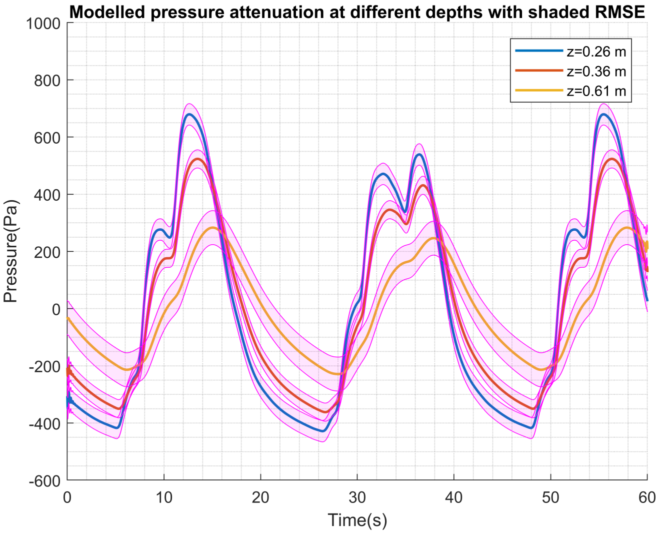

Figure 4.12: Modelled pressure for section 3, run 3, calibrated with a=32.5. The RMSE is purple shaded for each depth. The RMSE is 37, 32 and 59 for z=0.26 m, z=0.36 m and z=0.61 m, respectively.

4.3.3 Calibrated model results

The calibrated model results are discussed in this section. First, the pressure propagation of the model is compared to the observed data. Next, the pressure gradients are determined and the maximum pressure gradient at the bed surface is determined.

Pressure propagation

Figure 4.13 shows the pressure attenuation and phase lag. The pressure amplitude attenuation by increasing depth visually shows good alignments with the observed pressure from the wave flume experiment. Furthermore, the phase lag seems to be in the same order.

The relation of the modelled pressure with the observed pressure is studied in more detail by analysing the scatter plots. The modelled pressure is plotted against the observed pressure in a scatter plot. The R-squared correlation value is displayed for each depth. The x=y line indicates a perfect match between the modelled and observed pressure with $R^2 = 1$. Two cases are distinguished: one for positive pressure

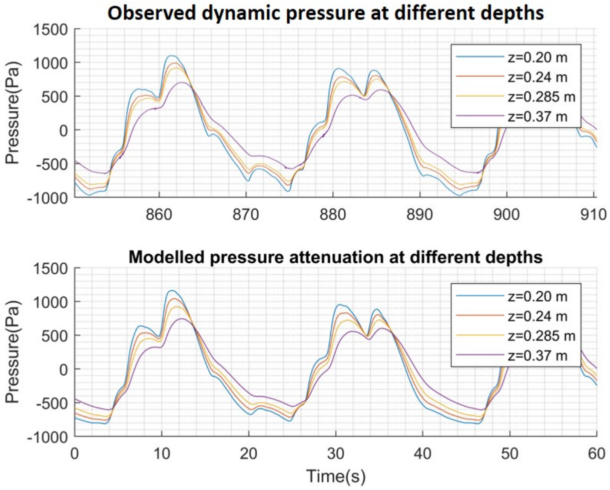

Figure 4.13: Pressure data from the wave flume experiment and modelled pressure data for section 2 with a=32.5 run 9.

values and one for negative pressure values. For positive pressure values the model underestimates the observed pressure when the scatter plot is greater than the x=y line. If the scatter plot is lower than the x=y line the model overestimates the observed pressure. In contrast, a lower scatter plot for negative pressure values underestimates the observed pressure by the model. From the scatter plots, the most interesting aspect are the limits clarify under or over estimation of the pressure amplitude peaks. For section 2, run 9 the model performs very well with a $R^2 = 0.99$ for each depth and no big outliers. The scatter plots for section 2 run 9 are displayed in Figure 4.14 and show high correlation degrees of $R^2 = 0.99$ for each depth. The modelled pressure amplitude peaks hardly show an over- or underestimation.

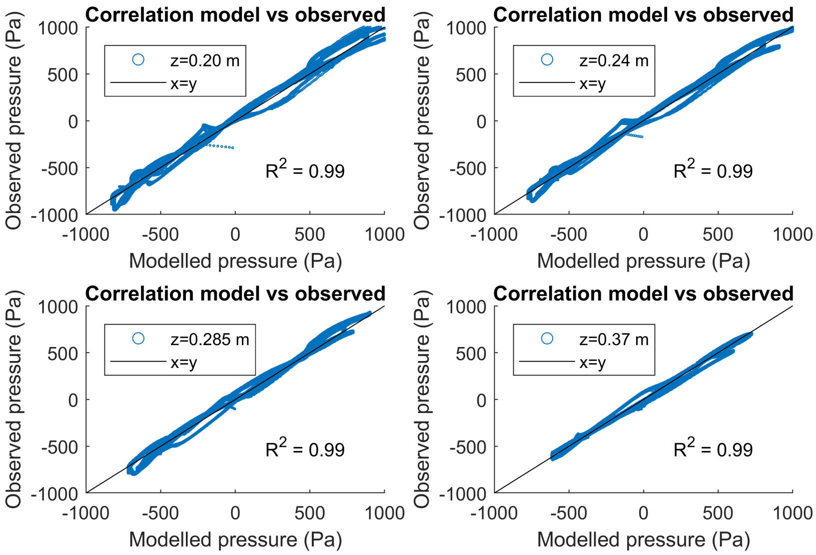

Figure 4.14: Scatter plots of the observed vs the modelled pressure. For section 2 with a=32.5 run 9.

The scatter plots for the other sections and runs are displayed in Appendix C. The correlation degree of $R^2 = 0.96$ for section 1 at depth z=0.20 m is one of the lowest. Also, the observed pressure amplitudes are bigger compared to the modelled pressure amplitudes. There might be an error in the bed surface level at section 1 during the run, possibly caused by the high scour depths reaching up to 7 cm.

Besides the qualitative analysis of the scatter plots, the under- and overestimation of the pressure amplitude peaks could be quantified by the normalized Root mean square error. Large deviations weight larger than small deviations, whereby pressure amplitude deviations will stand out.

Pressure gradient

The pressure gradient is analytically computed from the pressure propagation (3.13). Figure 4.15 shows the observed and modelled pressure gradient for $a = 32.5$. The data shows larger fluctuations in the pressure gradient between different depths caused by the inconsistent pressure amplitude attenuation. The pressure attenuation in depth for the modelled pressure behavior consists of gradual exponential steps and therefore less fluctuations are visible than for the observed pressure gradient. The magnitude of the pressure gradient gradually decreases by increasing depth.

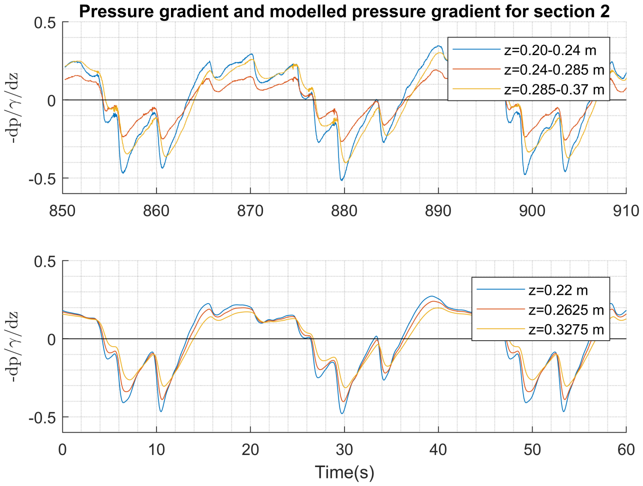

Figure 4.15: Pressure gradient normalized by the weight of water for a=32.5 run 9 and the wave surface elevation. When $-\frac{\frac{\partial p}{\gamma}}{\partial z} > 0$ there is an upwards directed pressure gradient.

Scatter plots are derived of the observed and modelled pressure gradients, displayed in Appendix C. The observed pressure gradients are determined by the central difference method in the midpoint between two depths. The pressure gradient is modelled in the midpoint. The large spatial distance in between the PPT's could lead to inaccuracies. The modelled pressure gradients for section 1 slightly underestimates the observed pressure gradient. In contrast to the small overestimation of the pressure gradient by the model for section 2 at depth $z = 0.3625m$ and $z = 0.4275m$. The pressure gradient for section 3 show good agreement for run 3. However, the modelled pressure gradient for a more eroded bed (run 9) is less accurate.

Pressure gradient close to the bed surface

The area of interest is the upper soil layer which is exposed by wave forcing on the bed. In this section the maximum pressure gradient close to the bed surface will be determined according to the model. The pressure at the bed surface $z = 0$ is analytically computed (3.13). Figure 4.16 shows the pressure gradient at the bed surface. The maximum upwards directed pressure gradient is in the order of $0.5\frac{Pa}{\gamma}/m$ equal to $4kPa/m$

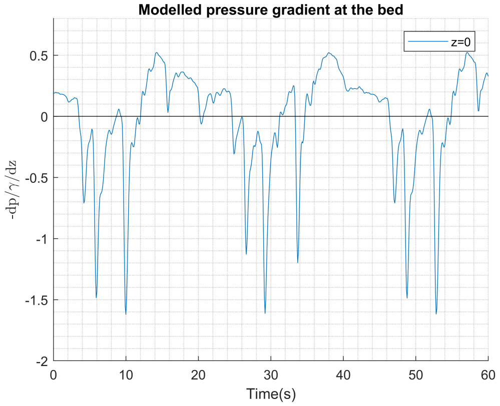

Figure 4.16: Pressure gradient close to the bed surface for a=32.5 run 9, section 2. When $-\frac{\partial \frac{p}{\gamma}}{\partial z} > 0$ there is an upwards directed pressure gradient.

4.3.4 Sensitivity analysis

A sensitivity analysis of both the bed surface level and the value for parameter a is performed. The uncertainty in the bed surface level influences the depth (z) of the PPT's relative to the bed surface level. This will change the depth dependent exponential amplitude attenuation. The bed surface level is varied in the range of $\pm 2.5cm$. The pressure amplitudes are normalized with the boundary pressure amplitude (P_0) to quantitatively analyse the amplitude change ratio. The value for parameter a is set to 32.5 and is varied ±5. The pressure amplitude attenuation depends on the depth and the wave number. The pressure amplitude attenuation ratio is determined for one wave group ($T_g = 22s$), displayed in Figure 4.17.

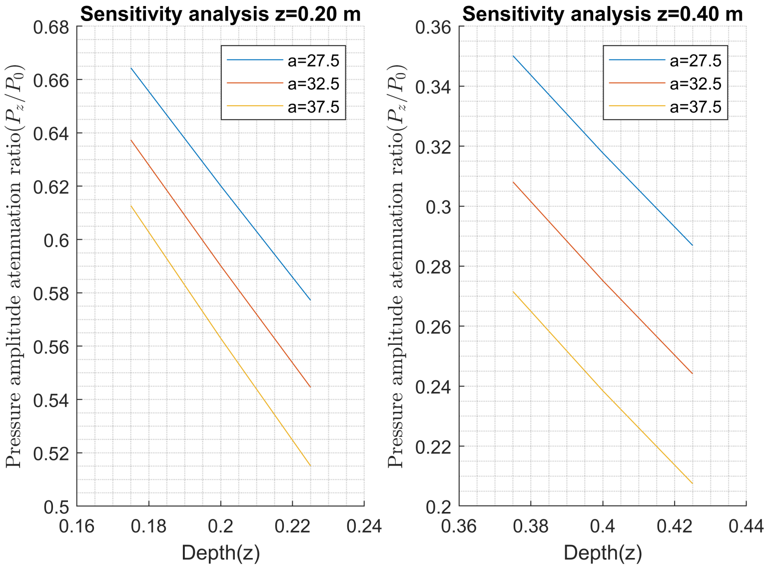

Figure 4.17: Sensitivity analysis bed surface level and parameter a for a wave group period of 22 s.

The pressure amplitude attenuation ratio for $z = 0.20m$ is 0.59. For $z = 0.175m$ and $z = 0.225m$ the pressure amplitude attenuation ratio is 0.64 and 0.54, respectively. This means that that pressure amplitude varies with ±5% within the range. For a larger depth the difference between $z = 0.40m$ and the varying bed surface level is only 3%. So, the uncertainty of the bed surface level at smaller depths influence the pressure amplitude more than on larger depths. This got to do with the relative error for smaller depths which is larger than for larger depths. For $z = 0.40m$ parameter value a is more sensitive than for the smaller depth $z = 0.20m$. Hence, the uncertainty in the bed surface level becomes of more importance for lower depths. The sensitivity of parameter a on a low depth is small, while parameter a is more sensitive on larger depths.

4.4 Sediment transport

The implication of pressure gradients on sediment transport is evaluated by using modified Shields methods. The outcomes for the different methods normalized by the Shields number are presented in this section. The seepage is computed from the pressure gradient and the permeability according to Darcy's law for one wave period of 42 seconds (2.2).

The two methods used are from Francalanci et al. (2008) and Nielsen et al. (2001). One of the input parameters is the permeability. The permeability does not influence the Shields number for the method of Francalanci et al. (2008), because the seepage, proportional to the pressure gradient times the permeability, is divided by the permeability. The permeability does play a role in the method of Nielsen et al. (2001). The determined permeability range is $K = 1.5 * 10^{-5} m/s$ according to the method of Kozeny-Carman and $K = 3.6 * 10^{-4} m/s$ for Hazen's method. Both values for the permeability are used in the modified Shields parametrizations of Nielsen et al. (2001) in order to estimate the sensitivity of the permeability. It turned out that a change of the permeability in this range has negligible effects (less than 0.1%) on the Shields number computation.

Another input parameter is the flow velocity, determined by the ADV's. The Shields number is computed for section 1 and 2. The wave conditions at section 3 are very similar to section 2. Both the flow velocity for run 3 and 9 are evaluated for both sections, showing periods of high fluctuations which indicate dry periods (Figure 4.18 and 4.19). Only for section 1 run 9 there are no dry periods. For section 2, high and low backwash velocities are observed compared to the uprush velocity, respectively. Positive velocities are onshore directed and negative velocities are offshore directed. The duration of the backwash period is longer than the uprush period. The high fluctuations indicate the periods of no inundation with no flow velocity. The bed shear stress at the bed as a function of the flow velocity is determined for each time step (2.6).

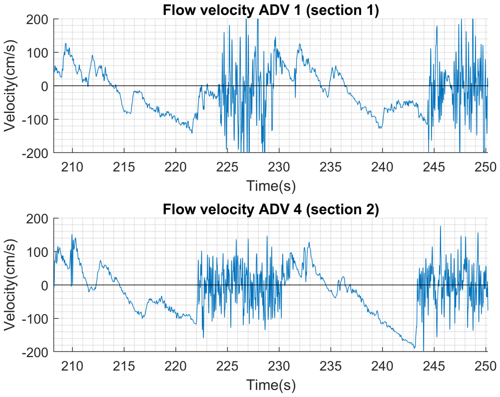

Figure 4.18: Flow velocity ADV 1 and 4 for run 3.

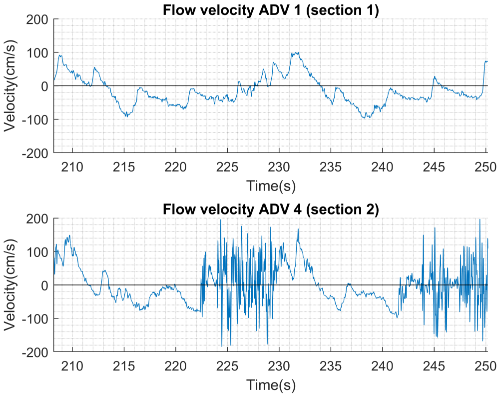

Figure 4.19: Flow velocity ADV 1 and 4 for run 9.

4.4.1 Normalized Shields methods

Both the method of Francalanci et al. (2008) and Nielsen et al. (2001) are used to compute the Shields number at each time step in the swash cycle for onshore and offshore velocities (2.16) (2.15). The modified Shields numbers are normalized by the original Shields number to quantitatively evaluate the effect of the method, displayed in Figure 4.20. The grey areas indicate the dry periods derived from the flow velocity plots. If there is no flow, sediment could not be transported and therefore the Shields number is not important at that time.

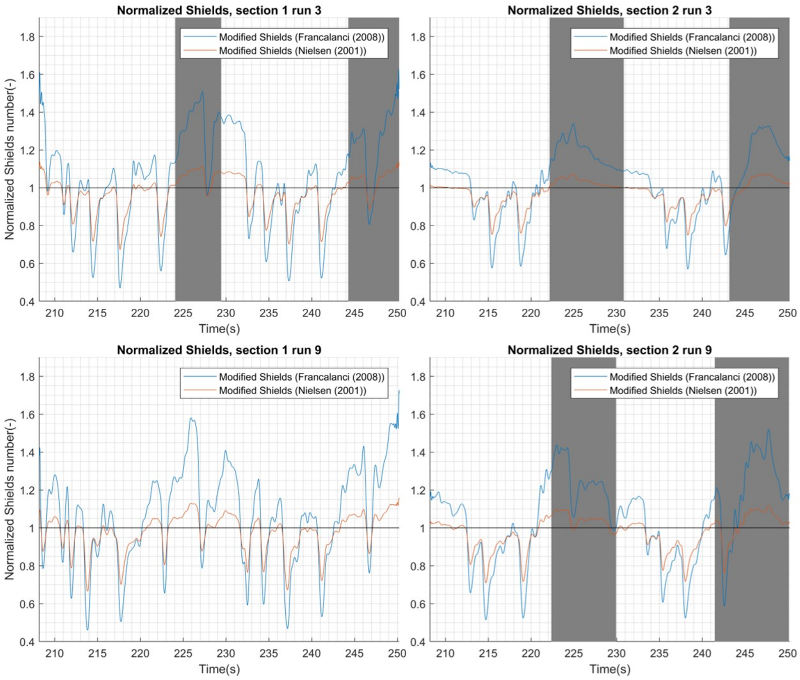

Figure 4.20: Normalized modified Shields for section 1 and 2 and run 3 and 9. The grey areas indicate the dry periods.

The maximum Shields number ratio's are 1.60 for Francalanci et al. (2008) and 1.13 for Nielsen et al. (2001) which is a very big difference. The maximum Shields number ratio's occur during backwash or dry periods. The minimum Shields number ratio's occur during uprush and are up to 0.5 for Francalanci et al. (2008) and 0.75 for Nielsen et al. (2001). The high Shields numbers occur during periods of low water levels or dry periods. The influence of the pressure gradient is the greatest in case of low water levels in between the wave groups, otherwise the sediment could not be transported. Nielsen et al. (2001) did incorporate both the change in effective sediment weight and the ventilated boundary layer effect. It turns out that the change of effective sediment weight has a bigger influence on the Shields number compared to the ventilated boundary layer effect for both the uprush and backwash stage. Lohmann et al. (2006) observed a bed shear stress decrease of 20% during exfiltration compared to a case without infiltration/exfiltration. The bed shear stress is linearly related to the Shields number. The effective sediment weight still will be leading over the ventilated boundary layer effect, when incorporating a bed shear stress decrease of 20% for the method of Francalanci et al. (2008). Section 1 run 9 is the only one for which the flow velocity is measured without fluctuations caused by no flow. In case of no flow, the Shields number is not useful, because the particles can not set into motion and be transported. The highest Shields numbers occur during dry periods. In case of no dry periods, the highest Shields number occurs during backwash. For a section and run without dry periods the implication for potential sediment transport is larger, because the duration of the backwash is larger and higher Shields numbers occur.

The sensitivity of the value for parameter a on the Shields number is evaluated. The flow velocity of section 1, run 9, is used and the value for parameter a is varied ±5 (Figure 4.21). For the method of Francalanci et al. (2008) maximum Shields numbers of approximately 1.5, 1.6 and 1.7 occur for $a = 27.5$, $a = 32.5$ and $a = 37.5$, respectively. For the method of Nielsen et al. (2001) maximum Shields numbers of approximately 1.11, 1.13 and 1.15 occur for $a = 27.5$, $a = 32.5$ and $a = 37.5$, respectively. So, a change in the value a within this range significantly effects the Shields number.

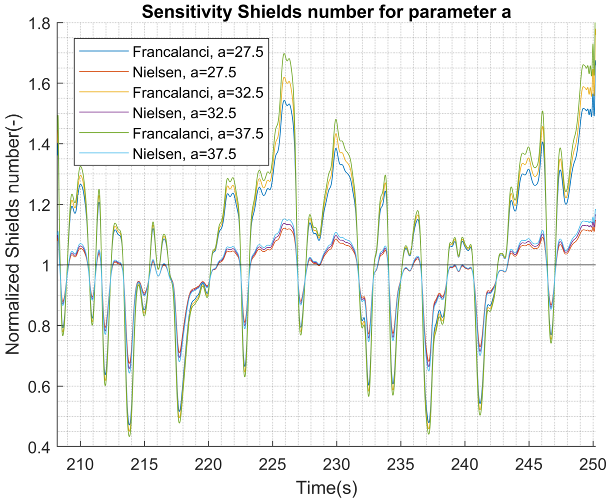

Figure 4.21: Normalized modified Shields for section 1 and 2 and run 3 and 9.

4.4.2 Liquefaction

The critical limit for liquefaction is computed assuming $\rho_s = 2650 kg/m^3$, $\rho = 1000 kg/m^3$ and $\varepsilon = 0.36$ the minimum vertical pressure gradient is in the order of $1e^4 Pa/m$ (2.8). The maximum pressure gradients for section 1 and 2 reaches up to an order of $5 * 10^3 Pa/m$. Half of the critical liquefaction threshold. However, the wave forcing at section 1 is more intense, so the possibility of liquefaction in the bed needs to be considered. The maximum upwards directed pressure gradient occurs when there is roughly no inundation. If the pressure gradient exceeds the threshold for liquefaction, a significant amount of sediment could be eroded 2.8.

Chapter 5

Discussion

In this chapter, the results that have been presented in the last chapter are discussed. The discussion is divided into three sections, starting with the observed wave and pressure behaviour and pressure gradients from the wave flume experiment. Next, the pressure propagation model is discussed. Finally, the chosen methods to determine the Shields number influenced by the pressure gradient are discussed.

5.1 Experiments

5.1.1 Observed wave and pressure behaviour

The pressure signal in the soil showed an exponential pressure amplitude attenuation and a linear phase lag by increasing depth. Low frequency waves travel further because less energy is transferred to the porous medium. In contrast to the high frequency waves, which damp faster, the small fluctuations in the wave surface elevation are not recognised in the pressure signal in the soil. The phase lag showed a linear relation by increasing depth for an individual frequency. This is consistent with the linear relation for partly saturated soils suggested by Yamamoto et al. (1978). However, the delay is frequency dependent and therefore the phase lag for the composed pressure signal does not necessarily have to be linear. Brajanovski et al. (2005) studied the wave-induced pressure propagation in a porous rock, with partly saturated pores and fractures, of a reservoir. The study shows that the stiffness of the medium (porous rock) can be very different for low and high frequencies. A different stiffness will result in different corresponding wave velocities, confirming that the wave velocities are frequency dependent. In comparison to this study, a different stiffness of the soil could clarify the frequency dependent wave velocities. A note of caution on the linear relation of the phase lag is that the relation is based on only four data points. Section 1 and 3 only have two and three data points, respectively, and therefore it is not possible to address a relation between the phase lag by increasing depth. Guest and Hay (2017) reported phase lags in between the bed surface and the pressure signal measured at z=0.50 m of 40-50 degrees for 0.26-0.31 Hz. This corresponds to a pressure propagation velocity of approximately 1.2 m/s. In this study, pressure propagation velocities for similar frequencies are approximately 0.4 m/s, which are a factor of three smaller. This is associated with a larger phase lag.

Surprisingly, the pressure sensors 6 and 7 for section 2, show similar pressure behaviour with a small pressure amplitude attenuation. The distance between PPT 8, 7 and 6 is 4 cm and 4.5 cm, respectively. A pressure amplitude attenuation at this depth would be proportional for almost an equal increase in depth, according to the theory. However, PPT 6 shows a dynamic pressure behaviour which is less attenuated than the model predicts for each run. On top of that, the linear phase lag for each frequency in between these two PPT's show a slightly different slope. These findings were unexpected. Also, the pressure gradients in between these two PPT's show contradicting results in comparison to the exponential pressure amplitude attenuation behaviour. It might suggest that this specific PPT, which is attached on the pole with tie wraps, was moved by the sediment placed on top.

5.1.2 Observed pressure gradients

The pressure gradient behaviour analysed in this study, was also reported by Sumer et al. (2013), showing graphs of a corresponding pressure gradient behaviour under one wave. The magnitude of the pressure gradients are difficult to compare due to the difference in burial depth. Sumer et al. (2013) used PPT's in the range from $z = 0.03 - 0.164$ m and the top soil measurements are used to determine the maximum $\frac{\partial p/y}{\partial z} = O(0.3)$ for a wave with a wave height of 5.9 cm and a period of 3.5 s. The waves in this study consist of multiple waves per group and larger wave heights, so at the bed surface the pressure gradients probably will be higher compared to Sumer et al. (2013). The modelled maximum pressure gradients at the bed are 2.5 times larger indeed (maximum $\frac{\partial p/y}{\partial z} = O(0.5)$).

5.2 Pressure propagation model

In comparison with the pressure modelling study of Guest and Hay (2017), which is also based on the theory of Yamamoto et al. (1978), the a values ($a = 2.9$) are one order of magnitude smaller. This difference is caused by the higher permeability associated with a sand-gravel-cobble beach in comparison to the medium to fine sandy beach, due to the larger grain sizes. Guest and Hay (2017) reported a permeability of $7.6 * 10^{-4}$ m/s. The smaller grain sizes of medium to fine sand will have a lower permeability. The permeability (k_c) and the bulk modulus (K') are sensitive parameters influencing the attenuation and phase lag. Guest and Hay (2017) addressed a doubling of the phase lag by decreasing the permeability by 75%. They also stated that by varying the porosity (n), the Young's modulus (E) and the Poisson's ratio (ν) within realistic ranges does negligible changes to the model output. So, the saturation degree (S_r), which influences the bulk modulus (K') and the permeability (k_c) highly determines parameter value a.

A risky assumption in the theory of Yamamoto et al. (1978), when used in the swash zone, is the constant saturation degree in depth and time. The swash zone is intermittently covered by water and exposed to the air, due to wave uprush and backwash. Therefore, the saturation of the bed changes in order of seconds. Despite this assumption, the calibrated model showed strong agreements with the observations.

The sensitivity of parameter value a and the uncertainty in the bed surface level on the pressure amplitude attenuation ratio is studied. The exact elevation of the bed surface becomes more important to determine the pressure amplitude attenuation for smaller depths. For a more eroded bed (run 9) it is more difficult to calibrate the model compared to a less eroded bed (run 3), due to the uncertainty in the bed surface level. The sensitivity of value a on the pressure amplitude attenuation ratio becomes more important for greater depths. At greater depths the uncertainty in the bed surface level is less sensible and therefore it is easier to calibrate the model.

In this study both Hazen's and Kozeny- Carman's methods are applied to compute the permeability within a range, based on the grain size distribution and the porosity. The grain size composition is not uniform and changes due to erosive waves. Eichentopf et al. (2020) analysed the cross-shore location dependent grain size distribution in a wave flume for sand with an equal grain size distribution of this study. Sediment sorting occurs at different locations, leading to different D_{10} values and roughly range from 0.15-0.25 mm. A D_{10} of 0.25 mm would increase the permeability by a factor of three for both methods. So, even if the grain size distribution in the soil layer at the sections is known, the uncertainty in the permeability at the bed surface remains due to sediment sorting. The sensitivity of the permeability on the Shields number is low, although the permeability highly influences the value of parameter a leading to different calibration values. It is important to bear in mind that the permeability is proportionally related to the parameter a value, so a factor of three difference in the permeability possibly causes a wider range of parameter a values. In this study, the fluctuation in parameter a values is not that large and ranges in between 30 and 37.5.

A validation is necessary whether a parameter value of $a = 30$ fits within the realistic regime of the physical soil characteristics. From Equations (2.12), (2.14) and (2.13) parameter a could be derived. For $S_r = 0.86$, $k_c = 1.9 * 10^{-4} m/s$, $n = 0.4$, $\gamma = 1 * 10^4 N$, $E = 30MPa$ and $\nu = 0.33$ at atmospheric pressure $a = 30$. The above mentioned parameter values are realistic parameters confirming that the calibration parameter of $a = 30$ is realistic.

5.3 Modified Shields formulations

Baldock and Nielsen (2010) discussed the validity of multiple Shields modifications based on the seepage, which induces a change in the effective sediment weight and/or the ventilated boundary layer. Two of the proposed methods are from Nielsen et al. (2001) and Francalanci et al. (2008). Baldock and Nielsen (2010) critically analysed the method proposed by Francalanci et al. (2008) which only incorporates the effective sediment weight. Still, this method is very useful to estimate the individual effect of the effective sediment weight on the Shields number. Cao et al. (2016) tried to validate the method of Nielsen et al. (2001) and Francalanci et al. (2008) on his experiments. The methods of Nielsen et al. (2001) and Francalanci et al. (2008) could not predict the sediment transport accurately. So, the applicability of both methods could be questioned and further research is needed to validate the methods. Nielsen et al. (2001) based the parameter value α on experiments from Conley and Inman (1994) from fixed beds, instead of real sand beds. Moreover, the bed friction factor from Conley and Inman (1994) was much smaller than for realistic sand beds. Therefore, the parameter value α is uncertain for this method. The modified Shields number is sensitive for parameter value a. The pressure amplitude attenuation and phase lag is captured in this parameter. These factors highly determine the magnitude of the pressure gradient and subsequently the Shields number.

The Shields number is an implication for sediment transport, although it is not possible to directly compare Shields numbers during uprush and backwash. Masselink and Hughes (1998) studied the proportionality factor for sediment transport depending on the Shields number. The proportionality factor is the term in front of the Shields number to compute the dimensionless average sediment transport which is different for uprush and backwash. The proportionality for uprush was twice as large compared to the backwash. Meaning that the the sediment transport rate is equal for a Shields number twice as big for backwash in comparison to uprush. There is no distinction between the types of flow for uprush and backwash. Besides the validity of the used methods, the methods do not incorporate all processes in the swash zone. Processes such as decelerating flow, presence of suspended sediment and wave collapse during uprush are not incorporated. Pedrozo-acuña et al. (2008) observed high spikes in the pressure on a steep gravel beach when the wave collapsed on the cross-shore location of a PPT, reaching up to 3 times the quasi-hydrostatic pressure defined as $\rho g H_s$. Besides the impact of the wave collapse, the wave breaking also enhances turbulence and vortices increasing the bed shear stress (Sumer et al., 2013).

For more extreme wave forcing conditions, the liquefaction potential is very important. Li et al. (2014) tested the pore pressure response on a storm surge event for multiple clay contents in a silty sea bed to indicate the probability of liquefaction in soil compositions. When the critical limit for liquefaction is exceeded, significant sediment transport takes place. Niu et al. (2019) experimentally showed that random waves caused stronger pore pressure response than regular waves. A larger duration in between wave groups could lead to an increase in the maximum upwards directed pressure gradient. Therefore, the liquefaction potential for bichromatic waves underestimates the true liquefaction potential. Irregular waves are more common to occur in nature.

Lastly, a uniform velocity profile is assumed in order to determine the bed shear stress. It is more likely that the velocity in the water column from the water surface to the bed decelerates due to the bed friction, although the main purpose, to derive a rough estimation of the flow velocity near the bed, is served by this assumption. However, with the available data it was not possible to approach the flow velocity near the bed.

Chapter 6

Conclusion

The aim of the research was to examine the observed pressure at different depths in the swash zone and to model the pressure propagation in the bed under wave uprush and backwash. Finally, the implication of the vertical pressure gradient in the soil on the sediment transport in the swash zone of a beach is evaluated. The stated research questions are answered below in order to achieve the research goal.

1. How does the vertical pressure gradient in the bed of the swash zone respond to wave forcing?

The pressure propagating through the bed showed a pressure amplitude attenuation by increasing depth with a linear phase lag. The pressure amplitude attenuation is in line with an exponential relation, by increasing depth. The linear phase lag is frequency dependent, with a smaller delay for high frequencies and has a pressure propagation velocity through the bed of approximately 0.4 m/s for the range of 0.26-0.31 Hz. The pressure amplitudes of high frequencies tend to attenuate faster compared to low frequencies, because less energy is transferred to the soil for low frequencies. The largest pressure gradients in the bed are present at the bed surface level due to the exponential pressure amplitude decay. The pressure gradient is directed downwards during uprush and directed upwards during backwash. The maximum upwards directed pressure gradient occurs during backwash or a dry period and decreases when the next wave approach the shore.

2. How can the pressure propagation and gradient in the bed be modelled as a response to the wave forcing?

The modelled pressure propagating through the porous bed according to the theory of Yamamoto et al. (1978) showed very good alignments with the observed pressure in the wave flume with a calibrated value of $a = 30 - 37.5$. The accuracy of fit of the modelled and observed pressure showed a correlation degree of at least $R^2 = 0.96$, Nash Sutcliffe values of 0.90 and Root Mean Square Errors, normalized by the standard deviation, of 0.31. The highest correlation degrees between the modelled and observed pressure are $R^2 = 0.99$, $NS = 0.99$, $RMSE/\sigma = 0.10$. The corresponding pressure gradients fit well ($R^2 = 0.95 - 0.99$), although the model tends to under- or overestimate the pressure gradients, if the correlation degree of the calibrated section is lower. These findings demonstrate the applicability of the theory of Yamamoto et al. (1978) for swash zone pressure propagating modelling. This is a powerful finding which can be used to determine the pressure gradients in the swash zone, based on the wave surface elevation and the soil characteristics.

3. What is the effect of the pressure gradient on the dimensionless bed shear stress (Shields number)?

The modelled pressure gradient at the bed is used in existing Shields parametrizations, to study the effect on the dimensionless bed shear stress. In this study, the magnitudes of the pressure gradients do not approach the critical liquefaction level under the wave forcing conditions and therefore the Shields formulation is applicable to determine the implication on sediment transport. The individual effect of the change in effective sediment weight and the combined effect of the effective sediment weight with the ventilated boundary layer, forced by the pressure gradient, is studied. High normalized Shields number ratio's are determined. They reach up to 1.6, during backwash, for the method of Francalanci et al. (2008), although the ventilated boundary layer effect is not incorporated in this method. This could cause a bed shear stress decrease of approximately (20%), due to the destabilizing effect of the exfiltration (Lohmann et al., 2006). Both effects are incorporated in the modified Shields parametrizations of Nielsen et al. (2001), directly showing the counter effect of both processes. The normalized Shields number ratio's, during exfiltration, increases up to 1.13. This study shows that the effective sediment weight effect is the leading process compared to the ventilated boundary layer effect and significantly influence the dimensionless bed shear stress (Shields number).

Finally, the three sub-questions are answered in order to draw conclusions on the main research question. There can be concluded that the pressure behaviour in the bed could be described with an exponential pressure amplitude attenuation and a linear phase lag by increasing depth. As a consequence, maximum upwards directed pressure gradients will occur during backwash or dry periods. Moreover, the findings approve the applicability of the theory of Yamamoto et al. (1978) to model the pressure propagation through the bed in the swash zone. Furthermore, the results of the implication of the pressure gradients on sediment transport show a significant influence on the dimensionless bed shear stress. Altogether, the findings of this study contribute to the research field of swash zone dynamics.

Chapter 7

Recommendations

A limitation of the experiment set up for this research is the burial depth of the pressure sensors. The area of interest is near the bed surface. Therefore, the pressure sensors should be placed closer to the bed surface to observe the pressure gradients at the bed surface, vulnerable for sediment transport. The pressure amplitude attenuation is determined in a small range of approximately 30 cm, in this study. Calibrating the model for the observed pressure signals in a broader range in depth will validate the applicability of the model under equal conditions. The applicability of the current model for the pressure propagation by increasing depth and the computation of the pressure gradient also can be validated for other swash zone experiments in a wave flume or a beach. When the model successfully simulates the pressure behaviour with a certain scaling parameter a, dependent on the soil characteristics, the model can be used as a tool to determine the pressure gradients for wave conditions common to occur in nature. A variety of wave patterns can be evaluated studying the pressure gradients and potential liquefaction.

The pressure response and the maximum pressure gradients under regular wave forcing are examined. Further experimental investigations are needed to observe the response for differently composed wave time series, varying the number of wave groups, waves per group and wave height. Random waves could provide more evidence on the influence of the duration in between the wave groups on the pressure gradient. In this study, the maximum upwards directed pressure gradient occurred in between the wave groups.

One source of weakness in this study, which could be prevented for future experiments, is the lack of knowledge on the permeability. The permeability is determined with empirical methods based on the porosity and the grain size. Laboratory tests with soil samples of the sediment could be performed to more accurately determine the permeability, at different locations in the swash zone. The driving factors for the pressure amplitude attenuation and phase lag are the permeability and the saturation degree. When the uncertainty in the permeability is smaller the saturation degree could be determined. Small changes in the permeability value do not have significant effects on the change of the Shields number for the modified Shields formulations used.

The precise mechanism of the ventilated boundary layer needs to be studied more extensively to determine the effect on the bed shear stress in the swash zone. Previous studies examined the ventilated boundary layer effect for a wave consisting of only one frequency. Exploring the ventilated boundary layer effect for a wave consisting of multiple frequencies in the swash zone is required to establish, whether the change in effective sediment weight is balanced by this process. A case study regarding the ventilated boundary layer in the swash zone under different infiltration/exfiltration rates compared to the situation without seepage will provide more evidence on the change in bed shear stress. Different permeable floors could be placed on the bed surface to examine the bed shear stress for different infiltration/exfiltration rates.

Bibliography

Anderson, D., Cox, D., Mieras, R., Puleo, J. A., and Hsu, T.-J. (2017). Observations of wave-induced pore pressure gradients and bed level response on a surf zone sandbar. *Journal of Geophysical Research: Oceans*, 122(6):5169–5193.

Bakhtyar, R., Ghaheri, A., Yeganeh-Bakhtiary, A., and Barry, D. (2009). Process-based model for nearshore hydrodynamics, sediment transport and morphological evolution in the surf and swash zones. *Applied Ocean Research*, 31(1):44–56.

Baldock, T. E. and Holmes, P. (1996). Pressure gradients within sediment beds. *Coastal Engineering*, pages 4161–4173.

Baldock, T. E. and Nielsen, P. (2010). Discussion of "effect of seepage-induced nonhydrostatic pressure distribution on bed-load transport and bed morphodynamics" by simona francalanci, gary parker, and luca solari. *Journal of Hydraulic Engineering*, 136(1):77–79.

Biot, M. A. (1941). General theory of three-dimensional consolidation. *Journal of Applied Physics*, 12(2):155–164.

Brajanovski, M., Gurevich, B., and Schoenberg, M. (2005). A model for P-wave attenuation and dispersion in a porous medium permeated by aligned fractures. *Geophysical Journal International*, 163(1):372–384.

Butt, T., Russell, P., Puleo, J., Miles, J., and Masselink, G. (2004). The influence of bore turbulence on sediment transport in the swash and inner surf zones. *Continental Shelf Research*, 24(7-8):757–771.

Cao, D., Chiew, Y. M., and Yang, S. Q. (2016). Injection Effects on Sediment Transport in Closed-Conduit Flows. *Acta Geophysica*, 64(1):125–148.

Carman, P. (1956). *Flow of Gases Through Porous Media*. Academic Press.

Carman, P. C. (1937). Fluid flow through granular beds. *Chemical Engineering Research and Design*, 75:S32–S48.

Chardón-Maldonado, P., Pintado-Patiño, J. C., and Puleo, J. A. (2016). Advances in swash-zone research: Small-scale hydrodynamic and sediment transport processes. *Coastal Engineering*, 115:8–25.

Conley, D. C. and Inman, D. L. (1994). Ventilated oscillatory boundary layers. *Journal of Fluid Mechanics*, 273(C6):261–284.

Eichentopf, S., van der Zanden, J., Cáceres, I., Baldock, T. E., and Alsina, J. M. (2020). Influence of storm sequencing on breaker bar and shoreline evolution in large-scale experiments. *Coastal Engineering*, 157(February):103659.

Elfrink, B. and Baldock, T. (2002). Hydrodynamics and sediment transport in the swash zone: a review and perspectives. *Coastal Engineering*, 45(3):149–167.

Francalanci, S., Parker, G., and Solari, L. (2008). Effect of seepage-induced nonhydrostatic pressure distribution on bed-load transport and bed morphodynamics. *Journal of Hydraulic Engineering*, 134(4):378–389.

Guest, T. and Hay, A. (2017). Vertical structure of pore pressure under surface gravity waves on a steep, megatidal, mixed sand-gravel-cobble beach. *Journal of Geophysical Research: Oceans*, 122:2647–2651.

Hazen, A. (1892). *Some Physical Properties of Sands and Gravels: With Special Reference to Their Use in Filtration.*

Horn, D. P. (2006). Measurements and modelling of beach groundwater flow in the swash-zone: a review. *Continental Shelf Research*, 26(5):622–652.

Kozeny, J. (1953). *Das Wasser im Boden. Grundwasserbewegung*, pages 380–445. Springer Vienna, Vienna.

Kozeny, M. (1927). Uber kapillare leitung des wassers im boden. *Sitzber. Akad. Wiss. Wein, Math-naturw*, 136:Abt. II a, P. 277.

Li, A., Luo, X., Lin, L., Ye, Q., and Le, C. (2014). An experimental study on the wave-induced pore water pressure change and relative influencing factors in the silty seabed. *Journal of Ocean University of China*, 13(6):911–916.

Lohmann, I. P., Fredsøe, J., Sumer, B. M., and Christensen, E. D. (2006). Large Eddy Simulation of the ventilated wave boundary layer. *Journal of Geophysical Research: Oceans*, 111(6).

Martin, C. S. and Aral, M. M. (1971). Seepage force on interfacial bed particles.

Masselink, G. and Hughes, M. (1998). Field investigation of sediment transport in the swash zone. *Continental Shelf Research*, 18(1998):1179–1199.

Masselink, G. and Li, L. (2001). The role of swash infiltration in determining the beachface gradient: a numerical study. *Marine Geology*, 176(1-4):139–156.

Masselink, G. and Puleo, J. A. (2006). Swash-zone morphodynamics. *Continental Shelf Research*, 26(5):661–680.

Nielsen, P., Robert, S., Møller-Christiansen, B., and Oliva, P. (2001). Infiltration effects on sediment mobility under waves. *Coastal Engineering*, 42(2):105–114.

Niu, J., Xu, J., Dong, P., and Li, G. (2019). Pore water pressure responses in silty sediment bed under random wave action. *Scientific Reports*, 9(1):1–11.

Pedrozo-acuña, A., Simmonds, D. J., and Reeve, D. E. (2008). Wave-impact characteristics of plunging breakers acting on gravel beaches. *Marine Geology*, 253:26–35.

Raubenheimer, B., Elgar, S., and Guza, R. (1998). Estimating wave heights from pressure measured in sand bed. *Waterway, Port, Coastal, And Ocean Engineering*, 124(June):151–154.

Reniers, A. J., Gallagher, E. L., MacMahan, J. H., Brown, J. A., Van Rooijen, A. A., Van Thiel De Vries, J. S., and Van Prooijen, B. C. (2013). Observations and modeling of steep-beach grain-size variability. *Journal of Geophysical Research: Oceans*, 118(2):577–591.

Rosas, J., Lopez, O., Missimer, T. M., Coulibaly, K. M., Dehwah, A. H., Sesler, K., Lujan, L. R., and Mantilla, D. (2014). Determination of hydraulic conductivity from grain-size distribution for different depositional environments. *Groundwater*, 52(3):399–413.

Shields (1936). Application of similarity principles and turbulence research to bed-load movement. Technical report.

Soulsby, R. (1998). Dynamics of Marine Sands (HR Wallingford Titles): A Manual for Practical Applications.

Sumer, B., Ari Guner, H., Hansen, N., Fuhrman, D., and Fredsoe, J. (2013). Laboratory observations of flow and sediment transport induced by plunging regular waves. *Journal of Geophysical Research: Oceans*, 118.

Sumer, B., Sen, M., Karagali, I., Ceren, B., Fredsoe, J., Sottile, M., Zilioli, L., and Fuhrman, D. (2011). Flow and sediment transport induced by a plunging solitary wave. *Journal of Geophysical Research*, 116.

Sumer, B. M. (2014). Liquefaction around marine structures. Technical report.

Turner, I. L. and Nielsen, P. (1997). Rapid water table fluctuations within the beach face: Implications for swash zone sediment mobility? *Coastal Engineering*, 32(1):45–59.

van der Werf, J., Dionísio António, S., Kranenborg, J., Vermeulen, B., Campmans, G., van der Zanden, J., Ribberink, J., Reniers, A., and Hulscher, S. (2019). Shaping The Beach: Cross-Shore Sand Transport in the Swash Zone. *Coastal Structures 2019*, pages 851–861.

van der Zanden, J. (2016). Sand Transport Processes in the Surf and Swash Zones. Technical report.

van der Zanden, J., Cáceres, I., Eichentopf, S., Ribberink, J. S., van der Werf, J. J., and Alsina, J. M. (2019). Sand transport processes and bed level changes induced by two alternating laboratory swash events. *Coastal Engineering*.

Waterways Experiment Station (1984). Shore protection manual. Technical report.

Yamamoto, T., Koning, H. L., Sellmeijer, H., and Van Hijum, E. V. (1978). On the response of a poro-elastic bed to water waves. *Journal of Fluid Mechanics*, 87(1):193–206.

Young, Y. L., Xiao, H., and Maddux, T. (2010). Hydro- and morpho-dynamic modeling of breaking solitary waves over a fine sand beach. Part I: Experimental study. *Marine Geology*, 269(3-4):107–118.

Appendix A

Data processing

The raw data is processed in order to use for further research. The calibration of the PPT's, interpolation, smoothing and fit equations are provided in this section.

A.1 Calibration PPT's

The PPT's are calibrated. Three different Mean Water Levels (MWL) of 2.453, 2.470 and 2.665 m determine the hydrostatic pressure, plotted relative to the pressure in Voltage. A linear line is fitted to the data points (Figure A.1), in order to determine the fitted function to convert the pressure data in Voltage to Pascal. The linear function fit for each PPT is displayed in Table A.1.

PPT number	PPT name	Linear fit equation
1	PPT_1040	$P = 2959V - 1276$
2	PPT_262	$P = 2507V + 504$
3	PPT_237	$P = 3970V + 927$
4	PPT_035	$P = 995V - 601$
5	PPT_1039	$P = 2689V - 394$
6	PPT_1038	$P = 2645V - 259$
7	PPT_1037	$P = 2625V - 353$
8	PPT_036	$P = 1042V - 234$
9	PPT_236	$P = 5016V - 571$
10	PPT_1041	$P = 3099V - 1067$
11	PPT_065	$P = 33088V - 14687$
12	PPT_058	$P = 1178V - 833$

Table A.1: Calibration PPT

PPT_065 (number 11), shows a linear fit with a big slope compared to the other PPT's. The sensor does not have a big reach in the Voltage signal (0.51-0.57 V). Therefore, the measurements are more inaccurate compared to the others. Because a small change in pressure possibly is not detected and the changes in pressure which will be detected are bumpy due to the relatively big bins covering the pressure signal. Therefore, the PPT is excluded from the data set.

A.2 Interpolation and smoothing

Preferably, the wave surface elevation signal of 40 Hz is upsampled to 100 Hz. Why? The resampling factor would be 5/2 and therefore a combination of interpolation and decimation is needed to obtain a rational factor. First, interpolate by a factor 5 and afterwards decimate by a factor 2. The water

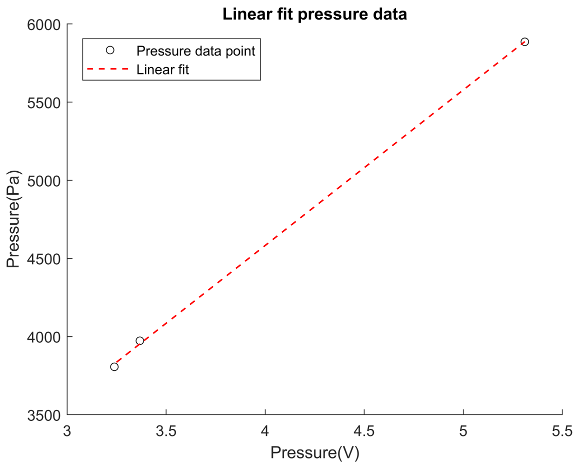

Figure A.1: Linear fit pressure data

surface elevation needs to be smoothed. Noise is caused by the acquisition system in the wave flume. The smoothing window is chosen such that the noise is extracted (Figure A.2). The pressure data does not require smoothing.

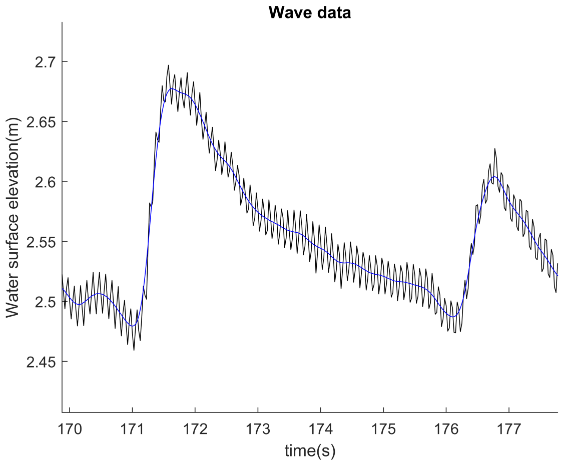

Figure A.2: Smoothed water surface elevation

A.3 Polynomial fit equations phase lag

The polynomial fit equations for the phase lag in between the PPT's of section 2 are displayed below. From PPT 8-5, PPT 8-6 and PPT 8-7.

$$fit(x) = 30x^3 - 60x^2 + 190x + 13 \tag{A.1}$$

$$fit(x) = 12x^3 - 26x^2 + 54x + 7 \tag{A.2}$$

$$fit(x) = 11x^3 - 16x^2 + 30x + 5 \tag{A.3}$$

Appendix B

Model calibration

The

B.1 Depth PPT's

The bed surface level for run 3 and 9 for section 2 and 3 is determined based on the measured profiles and scour after a run B.1. This enables us to determine the depths of the PPT's B.2.

Run	**Reference point**	**Section 1 (m)**	**Section 2 (m)**	**Section 3 (m)**
	Original bed surface elevation relative to MWL	-0.091	0.043	0.105
3	Surface elevation after run 80 relative to MWL	-0.128	-0.0175	0.055
	Scour depth	-0.05	-0.01	-0.01
	Erosion depth relative to original bed surface	0.087	0.053	0.042
9	Surface elevation after run 86 relative to MWL	-0.225	-0.12	-0.027
	Scour depth	-0.07	-0.01	-0.025
	Erosion depth relative to original bed surface	0.204	0.154	0.157

Table B.1: Erosion at sections 2 and 3 at the beginning of run 3 and 9.

Run	**Section 1**		**Section 2**				**Section 3**		
	PPT_2	PPT_1	PPT_8	PPT_7	PPT_6	PPT_5	PPT_12	PPT_10	PPT_9
	z (m)	z (m)	z (m)	z (m)	z (m)	z (m)	z (m)	z (m)	z (m)
Original	0.40	0.50	0.35	0.39	0.435	0.52	0.30	0.40	0.65
3	0.31	0.41	0.30	0.34	0.385	0.47	0.26	0.36	0.61
9	0.20	0.30	0.20	0.24	0.285	0.37	0.14	0.24	0.49

Table B.2: Depth PPT's relative to the bed surface at section 2 and 3 at the beginning of run 3 and 9

B.2 Calibrated model

Based on the goodness of fit methods, the model is calibrated for run 3 and 9 for section 2 (Table B.4) and section 3 (Table B.5. Resulting in a values for section 2 of 37.5 and 32.5 for run 3 and 9, respectively. For section 3, a values of 32.5 for both runs. For section 3 the biggest error is found for the deepest PPT.

	Method	PPT_2	PPT_1
Run 3			
a=35	RMSE/σ	0.3072	0.2587
	NS	0.9056	0.9331
a=40	RMSE/σ	0.3113	0.2654
	NS	0.9031	0.9296
a=37.5	RMSE/σ	0.2794	0.2634
	NS	0.9220	0.9306
Run 9			
a=35	RMSE/σ	0.2675	0.2977
	NS	0.8787	0.9403
a=20	RMSE/σ	0.3137	0.2320
	NS	0.9284	0.9113
a=32.5	RMSE/σ	0.3483	0.2443
	NS	0.8891	0.9431
a=27.5	RMSE/σ	0.3026	0.2403
	NS	0.9084	0.9422
a=30	RMSE/σ	0.3330	0.2384
	NS	0.9016	0.9462

Table B.3: Calibrated a value at section 1 for run 3 and 9. Based on the Root Mean Square Error divided by the standard deviation of the observed pressure signal and the Nash Sutcliffe coefficient.

	Method	PPT_8	PPT_7	PPT_6	PPT_5
Run 3					
a=30	RMSE/σ	0.1631	0.1754	0.1324	0.1925
	NS	0.9734	0.9692	0.9825	0.9629
a=40	RMSE/σ	0.1245	0.1171	0.1568	0.1286
	NS	0.9845	0.9863	0.9754	0.9835
a=35	RMSE/σ	0.1238	0.1214	0.1152	0.1142
	NS	0.9847	0.9853	0.9867	0.9870
a=37.5	RMSE/σ	0.1193	0.1126	0.1318	0.1099
	NS	0.9858	0.9873	0.9826	0.9879
Run 9					
a=30	RMSE/σ	0.2056	0.1845	0.1951	0.1398
	NS	0.9577	0.9660	0.9619	0.9804
a=40	RMSE/σ	0.1564	0.1523	0.1966	0.1460
	NS	0.9755	0.9768	0.9613	0.9787
a=35	RMSE/σ	0.1268	0.1162	0.1460	0.0870
	NS	0.9839	0.9865	0.9787	0.9924
a=32.5	RMSE/σ	0.1046	0.0999	0.0941	0.0912
	NS	0.9891	0.9900	0.9912	0.9917

Table B.4: Calibrated a value at section 2 for run 3 and 9. Based on the Root Mean Square Error divided by the standard deviation of the observed pressure signal and the Nash Sutcliffe coefficient.

	Method	PPT_12	PPT_10	PPT_9
Run 3				
a=30	RMSE/σ	0.1074	0.1008	0.2376
	NS	0.9885	0.9898	0.9435
a=35	RMSE/σ	0.0807	0.0556	0.3517
	NS	0.9935	0.9969	0.8763
a=32.5	RMSE/σ	0.0882	0.0665	0.2971
	NS	0.9922	0.9956	0.9117
Run 9				
a=30	RMSE/σ	0.2400	0.1843	0.2277
	NS	0.9424	0.9660	0.9482
a=40	RMSE/σ	0.1851	0.1202	0.3980
	NS	0.9657	0.9855	0.8416
a=35	RMSE/σ	0.2090	0.1400	0.3177
	NS	0.9563	0.9804	0.8991
a=32.5	RMSE/σ	0.2236	0.1594	0.2737
	NS	0.9500	0.9746	0.9251

Table B.5: Calibrated a value at section 3 for run 3 and 9. Based on the Root Mean Square Error divided by the standard deviation of the observed pressure signal and the Nash Sutcliffe coefficient.

Appendix C

Scatter plots observed vs modelled pressure

The scatter plots of the calibrated three sections for run 3 and 9 are displayed in this section. The observed pressure is plotted against the modelled pressure and the correlation degree (R^2) is given for each depth. The input in the scatter plot is the data from four swash cycles with a total duration of 168 s. furthermore, the scatter plots of the pressure gradients are displayed.

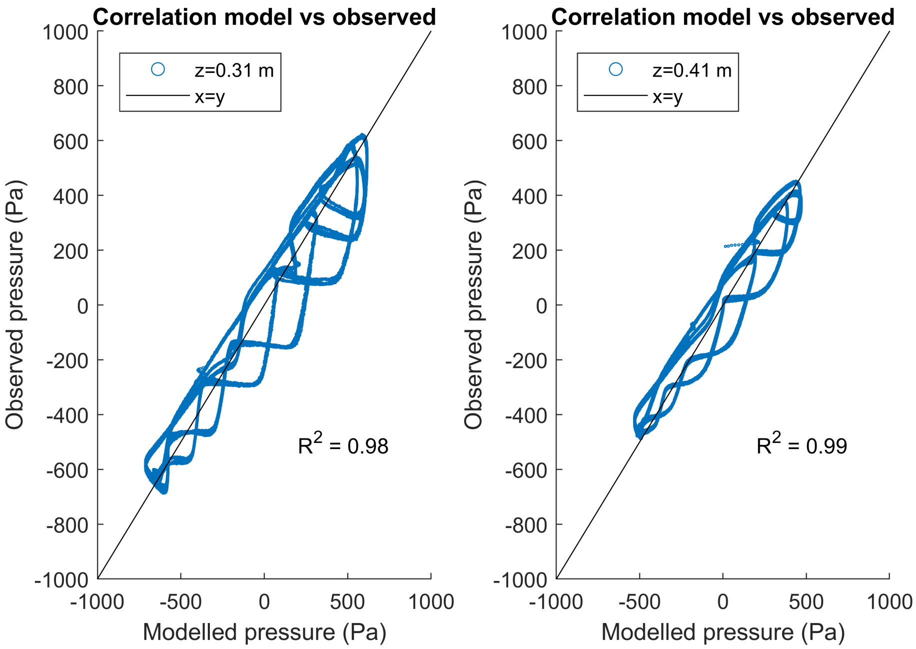

Figure C.1: Scatter plots of the observed vs the modelled pressure for section 1 with a=37.5 run 3.

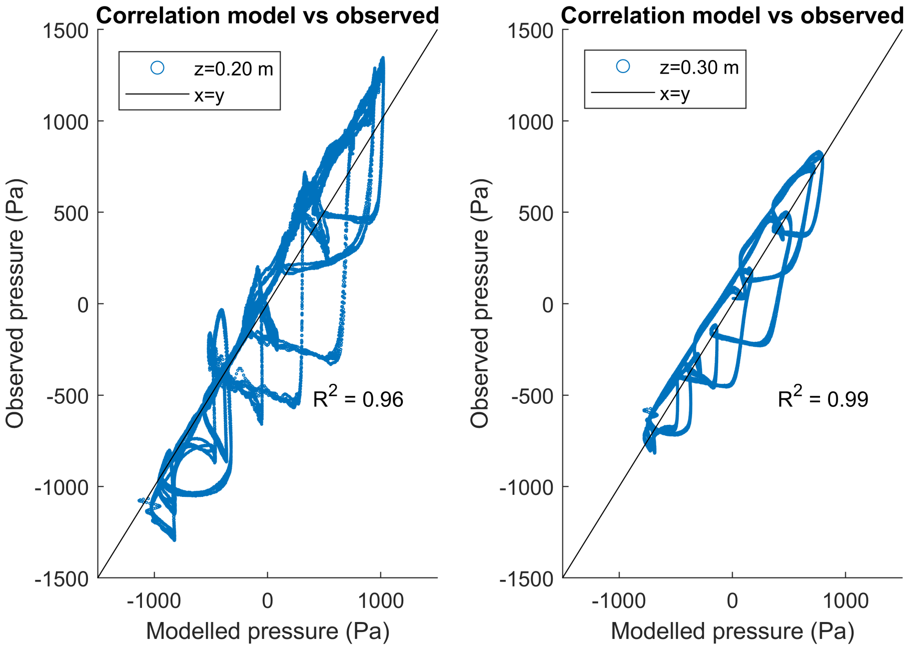

Figure C.2: Scatter plots of the observed vs the modelled pressure for section 1 with a=30 run 9.

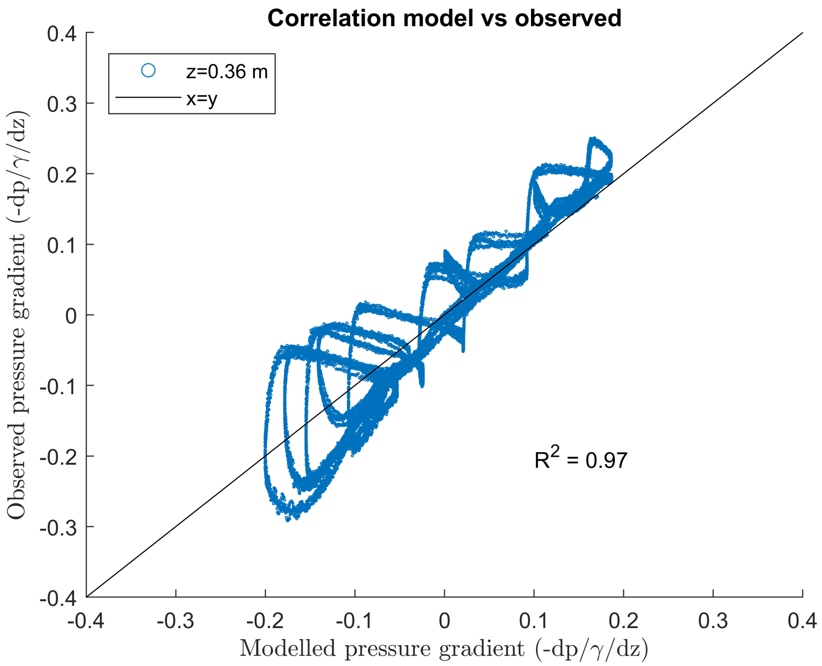

Figure C.3: Scatter plots of the observed vs the modelled pressure gradient for section 1 with a=37.5 run 3.

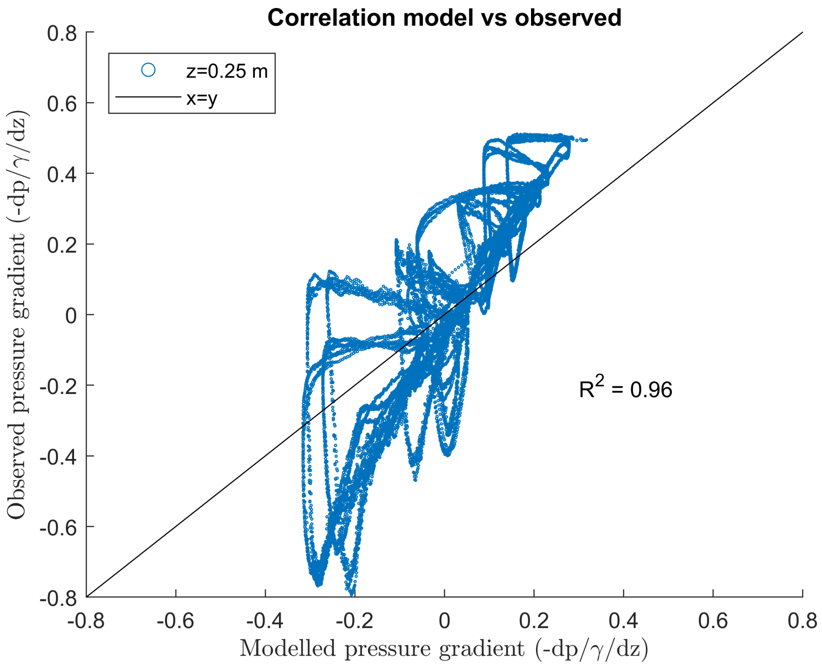

Figure C.4: Scatter plots of the observed vs the modelled pressure gradient for section 1 with a=30 run 9.

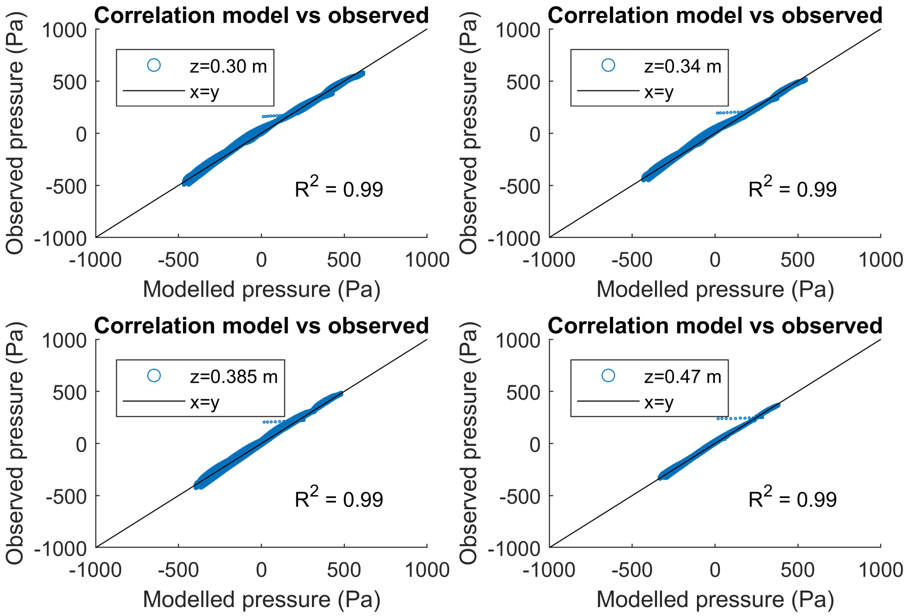

Figure C.5: Scatter plots of the observed vs the modelled pressure for section 2 with a=37.5 run 3.

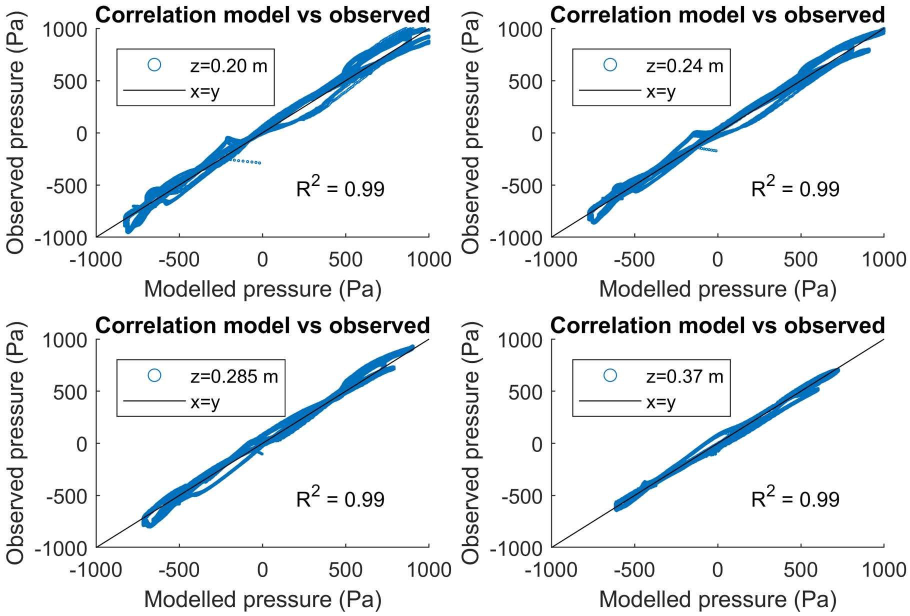

Figure C.6: Scatter plots of the observed vs the modelled pressure for section 2 with a=32.5 run 9.

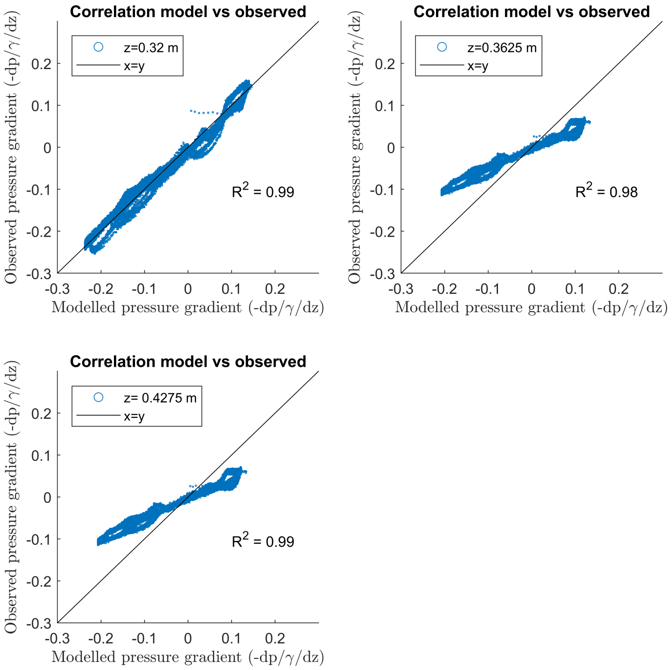

Figure C.7: Scatter plots of the observed vs the modelled pressure gradient for section 2 with a=37.5 run 3.

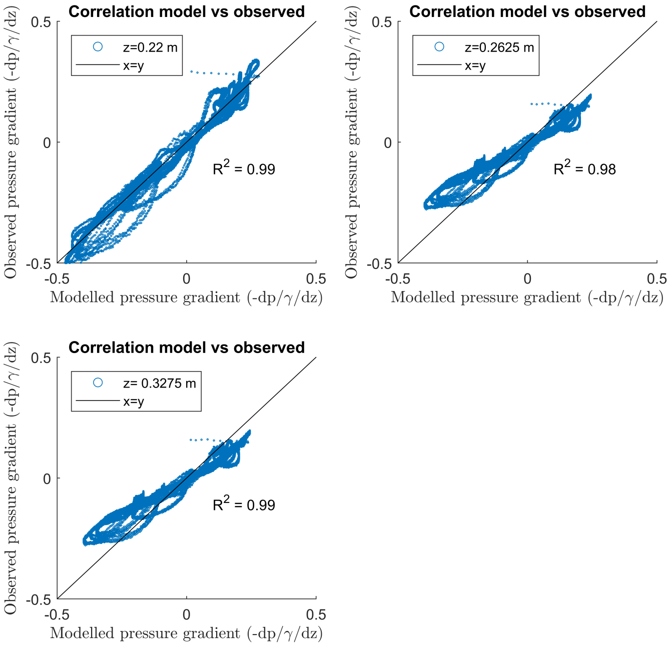

Figure C.8: Scatter plots of the observed vs the modelled pressure gradient for section 2 with a=32.5 run 9.

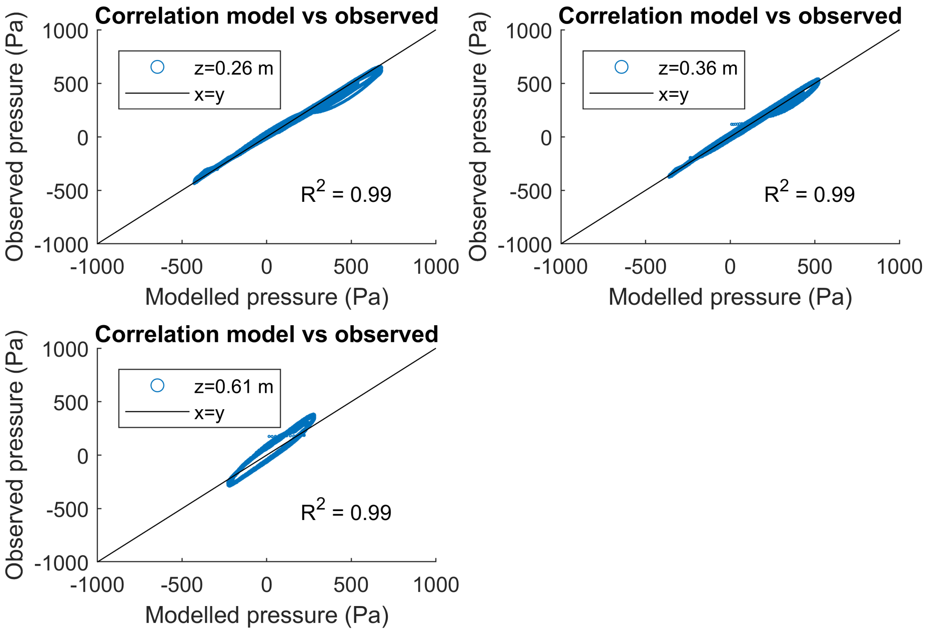

Figure C.9: Scatter plots of the observed vs the modelled pressure for section 3 with a=32.5 run 3.

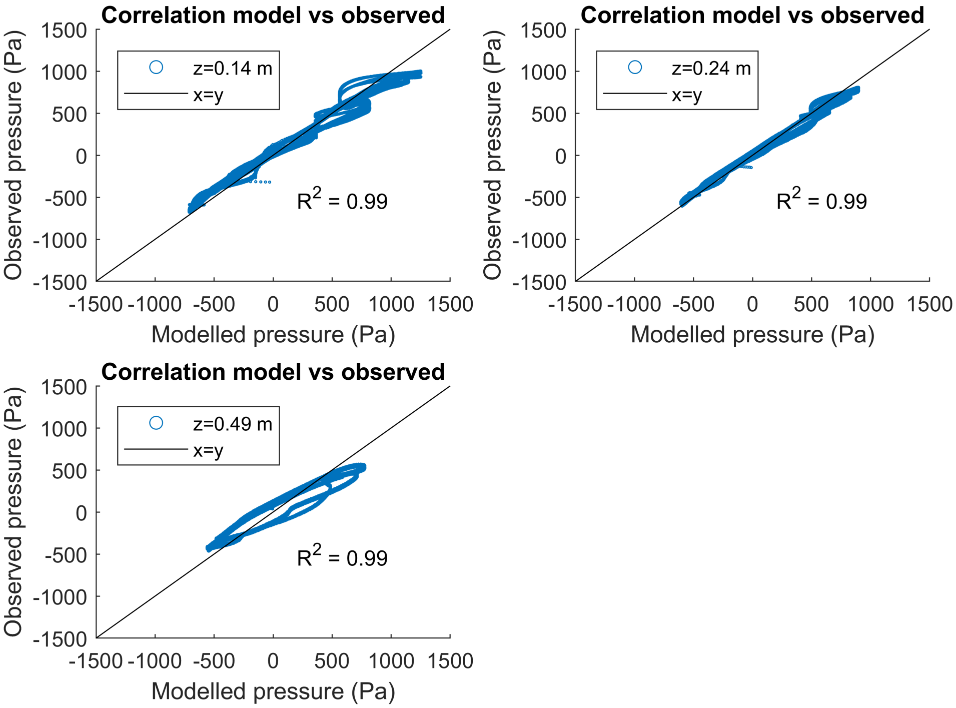

Figure C.10: Scatter plots of the observed vs the modelled pressure for section 3 with a=32.5 run 9.

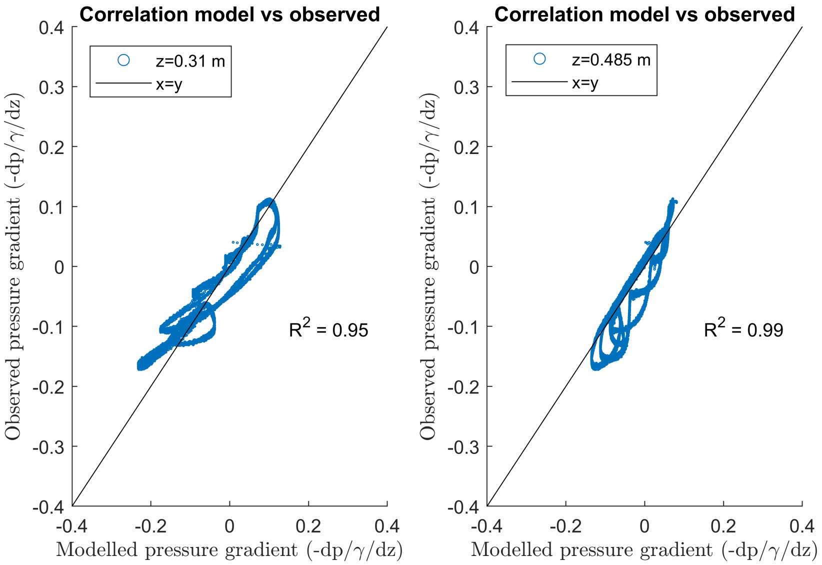

Figure C.11: Scatter plots of the observed vs the modelled pressure gradient for section 3 with a=32.5 run 3.

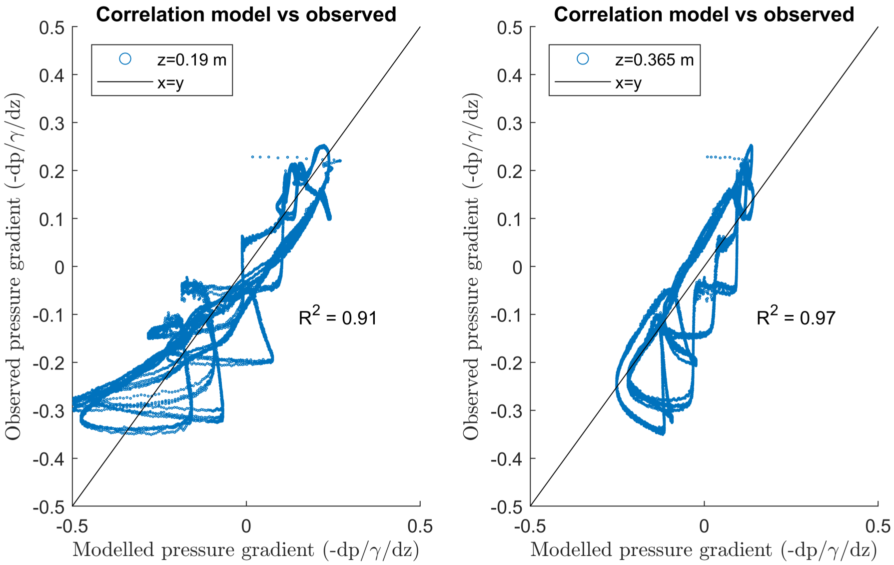

Figure C.12: Scatter plots of the observed vs the modelled pressure gradient for section 3 with a=32.5 run 9.